

Chapter 22

Metamaterials

Petr Kužel and Hynek Němec

Abstract We provide an overview of the THz research in metallic and dielectric metamaterials. We introduce the appropriate length scales and averaging procedures to define effective metamaterial properties. A broader discussion of elaboration technologies and experimental determination of metamaterial properties is provided. Finally, we focus on applications aiming to achieve negative refractive index and active control of THz light.

22.1 Introduction and a Few Historical Remarks

Electromagnetic metamaterials are man-made structures which can exhibit specific on-demand electric and/or magnetic response not found in natural materials. These structures are usually periodic with the period and the motive much smaller than the wavelengths of the targeted spectral range, typically $< \lambda/10$. This condition being fulfilled, the response of metamaterials is essentially due to individual resonances of structured patterns within the unit cell which can be described by effective (averaged) material parameters: usually by the effective dielectric permittivity ε and magnetic permeability μ .

Historically, the first targeted applications concerned the phenomena related to the negative refractive index which requires simultaneously negative ε and μ . Some of these phenomena had been first predicted by Veselago [1]. Nevertheless, the general interest of the scientific community in metamaterials, which has arisen much later, is mainly due to the pioneering work of Pendry who introduced the metamaterial concept by showing the way to decrease the plasma frequency of metals down to microwave and terahertz range [2, 3] and how to achieve the negative effective permeability at microwaves [4]. He also proposed and theoretically demonstrated

P. Kužel (✉) · H. Němec
Institute of Physics, Academy of Sciences of the Czech Republic, Prague, Czech Republic
e-mail: kuzelp@fzu.cz

the principle of a superlens, a slab with negative refraction allowing one to achieve a subwavelength spatial resolution [5]. The word “metamaterial” first appeared in the paper by Smith et al. in 2000 [6], where the first structured material with simultaneously negative permeability and permittivity was demonstrated at microwave frequencies. The first real breakthrough in the terahertz metamaterial science came about 4 years later: in 2004, Yen et al. [7] demonstrated a planar structure exhibiting a range of negative effective magnetic permeability. Later, an equally important paper on THz metamaterials was published by Chen et al. [8]. Here, the authors show that, besides the negative refraction, there are other perspectives for metamaterial applications in the THz technology; namely, external control of the metamaterial resonances (their spectral tuning or switching on/off) promises great potential for the manipulation of the terahertz light.

During the past several years a number of books have been published focusing on the properties and design of metamaterials [9–11] that the interested reader may consult. In this chapter, after an introduction discussing different regimes of the electromagnetic response of structured matter, we provide merely the main advances in metamaterial science developed in the THz spectral region during the past few years. We also attract the reader’s attention to a recently published review on the manipulation of terahertz radiation using metamaterials [12].

22.2 Length Scales: Averaging of Electric and Magnetic Quantities

22.2.1 Atomic Scale

Microscopically, the classical electromagnetic theory describes the electromagnetic field and its interaction with matter which consists of an ensemble of charged particles. The field which enters into play is local and may vary by many orders of magnitude on a nanoscopic scale (namely in the vicinity of charges). The coupling between charges and the field is described by Maxwell–Lorentz equations for the local electric field \mathbf{e} and magnetic induction \mathbf{b} :

$$\begin{aligned}\nabla \cdot \mathbf{e} &= \frac{\rho}{\varepsilon_0} \\ \nabla \cdot \mathbf{b} &= 0 \\ \nabla \times \mathbf{e} + \frac{\partial \mathbf{b}}{\partial t} &= 0 \\ \frac{1}{\mu_0} \nabla \times \mathbf{b} - \varepsilon_0 \frac{\partial \mathbf{e}}{\partial t} &= \mathbf{j}\end{aligned}\tag{22.1}$$

where \mathbf{j} and ρ denote the local current and density of charge, respectively. Employing classical mechanics picture of point charges, these quantities have a discrete nature expressed by Dirac δ -functions:

$$\begin{aligned}\rho(\mathbf{r}, t) &= \sum_{\alpha} q_{\alpha} \delta(\mathbf{r} - \mathbf{r}_{\alpha}(t)) \\ \mathbf{j}(\mathbf{r}, t) &= \sum_{\alpha} q_{\alpha} \mathbf{v}_{\alpha} \delta(\mathbf{r} - \mathbf{r}_{\alpha}(t)).\end{aligned}\quad (22.2)$$

The solution of the electromagnetic problem, i.e., of Eqs. (22.1) and (22.2) supplemented by the Lorentz force $\mathbf{f} = \rho\mathbf{e} + \mathbf{j} \times \mathbf{b}$, on a macroscopic scale would imply finding the positions (and their time evolution) of a huge number of charges. This is not feasible and also such detailed information is not needed for practical applications. It is then convenient to proceed to a space averaging of the local quantities on the atomic scale [13, 14]. The appropriate scale for this averaging is ~ 10 nm, which means that this concept is valid up to the frequencies of radiation in the vacuum UV spectral range ($\lambda \gg 10$ nm). The local response of the charges (current of free charges and dipolar polarization of the bound charges) can then be accounted for by complex and frequency-dependent material parameters ε (dielectric permittivity) and μ (magnetic permeability) which describe the macroscopic polarization \mathbf{P} and magnetization \mathbf{M} of the medium and connect the spatially averaged vector fields $\mathbf{E} = \langle \mathbf{e} \rangle$ and $\mathbf{B} = \langle \mathbf{b} \rangle$ to newly introduced vectors \mathbf{D} and \mathbf{H} :

$$\begin{aligned}\mathbf{D}(\omega) &= \varepsilon(\omega) \mathbf{E}(\omega) = \varepsilon_0 \mathbf{E} + \mathbf{P} \\ \mathbf{B}(\omega) &= \mu(\omega) \mathbf{H}(\omega) = \mu_0 (\mathbf{H} + \mathbf{M})\end{aligned}\quad (22.3)$$

which should satisfy the Maxwell equations for macroscopic fields:

$$\begin{aligned}\nabla \cdot \mathbf{D} &= 0 \\ \nabla \cdot \mathbf{B} &= 0 \\ \nabla \times \mathbf{E} + \frac{\partial \mathbf{B}}{\partial t} &= 0 \\ \nabla \times \mathbf{H} - \frac{\partial \mathbf{D}}{\partial t} &= 0\end{aligned}\quad (22.4)$$

The quantities \mathbf{e} and \mathbf{b} contain the near-field information, i.e., the behavior of local fields on the atomic scale, while the vectors \mathbf{E} , \mathbf{D} , \mathbf{H} , \mathbf{B} describe correctly the far field but we cannot use them to retrieve the near field.

Note that in this chapter we use the convention where the harmonic wave in the complex notation is described by the phase factor $\exp(+i\omega t)$ and the complex material response is then given by $\varepsilon = \varepsilon' - i\varepsilon''$, $\mu = \mu' - i\mu''$.

The dielectric polarization of media is connected to a dynamical separation of bound charges which define the electric dipole moments; the magnetic polarization in materials then arises from the orbital currents or from unpaired electron spins. The characteristic distances and sizes of the current loops are then on sub-nm scale which may impose some limits to the strength of the resonant interaction with the field. Namely, the resonant phenomena in magnetic systems tend to occur in the

microwave range which results in an absence (or at least weakness) of the natural magnetic material response at THz frequencies.

Patterning the materials brings another length scale into play. The macroscopic fields on the atomic scale may now regain a local character with respect to the length scale of the newly introduced inhomogeneity (artificial structure). Patterns within the unit cell of the metamaterial structure can be considered as artificial metamaterial atoms characterized by electric and magnetic dipolar moments which are now defined not only by the material used but also by the geometry, i.e., by the extent of the possible charge separation and by the area of the surface delimited by the current loops. The size of the unit cell is chosen to be substantially smaller than the targeted wavelength and, at the same time, much larger than the interatomic distances. On the one hand, at the length scale of the wavelength the meta-atoms constitute elementary electric and magnetic dipole moments which can be macroscopically described by effective permeability and permittivity obtained by an averaging procedure (analogous to that used at the atomic scale); on the other hand, the magnitudes of the dipoles may significantly exceed those observed on the atomic scale and the positions of the resonant frequencies can be tailored by the geometry and the length scale of the structure.


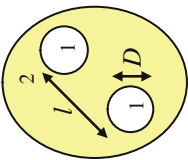
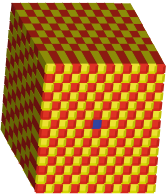
The important parameters are the dimensions of the unit cell and of the individual meta-atoms (denoted by l and D respectively, in the schemes in Table 22.1) or, more precisely, their ratios to the wavelength. We may distinguish three different regimes which are described below and summarized in Table 22.1; two of them are of concern for the physics discussed in this chapter.

22.2.2 Composites

By composites we mean here the structures which can be described within a static approximation which involves the standard effective medium theory (column 2 in Table 22.1). For example, if we consider a purely dielectric composite, then the electromagnetic field can be considered as almost homogeneous inside the dielectric inclusions. This is expressed by the conditions for the applicable radiation wavelengths $\lambda \gg \sqrt{\varepsilon_2}l$ and $\lambda \gg \sqrt{\varepsilon_1}D$ in Table 22.1. We do not expect any additional geometry-related resonances in this spectral range and the medium can be described by effective medium approximation (EMA). Within this approximation the effective permittivity of the composite is evaluated in terms of the dielectric functions of the components, of their shape, and of their volume fractions. No anomaly of the magnetic permeability is expected here ($\mu_{\text{eff}} \approx 1$) if we deal with intrinsically non-magnetic components. The two most widely used effective medium models are the Maxwell–Garnett model [15]:

$$\frac{\varepsilon_{\text{eff}} - \varepsilon_2}{\varepsilon_{\text{eff}} + \eta\varepsilon_2} = f \frac{\varepsilon_1 - \varepsilon_2}{\varepsilon_1 + \eta\varepsilon_2} \quad (22.5)$$

Table 22.1 Inhomogeneities on various length scales compared to the wavelength and their description. (EMA = effective medium approximation)

Category	Atomic scale ~ 10 nm	Composites	Metamaterials	Photonic crystals
Scheme				
Microscopic description	e, b	Dielectric or metallic inclusions: l, D, ϵ_i (or σ_i)	Extension of EMA (Mie scattering theory) other homogenization procedures	Periodic ϵ
Macroscopic description	Averaging: E, B, D, H	EMA (Maxwell–Garnett, Bruggeman...)	$\lambda \gg \sqrt{\epsilon_2}l, \sqrt{\epsilon_2}D$ $\lambda \gg \sqrt{\epsilon_1}D$	Band structure
Validity of macroscopic description	$\lambda \gg 10$ nm	$\epsilon_{\text{eff}} (\mu_{\text{eff}} = 1)$	$\epsilon_{\text{eff}}, \mu_{\text{eff}}$	$\lambda \approx \sqrt{\epsilon}l$
Effective parameters	ϵ, μ	Dielectrics; no geometrical resonance metals; plasmonic resonance	Each element is individually resonant no coupling between elements	—
Origin of resonant behavior	Polarization of bound charges orbital currents, spins			Resonances due to interferences coupling between periodically distributed elements
Reciprocal space (reciprocal parameter G)	—	$0 \approx \omega/c \ll G$	Below the first bandgap $\omega/c < G$	Band structure with bandgaps spatial dispersion of the photonic crystal

and the Bruggeman model [16]:

$$f \frac{\varepsilon_1 - \varepsilon_{\text{eff}}}{\varepsilon_1 + \eta \varepsilon_{\text{eff}}} + (1 - f) \frac{\varepsilon_2 - \varepsilon_{\text{eff}}}{\varepsilon_2 + \eta \varepsilon_{\text{eff}}} = 0 \quad (22.6)$$

where f is the volume filling fraction of the ε_1 material in the composite, η is the shape factor ($\eta = 2$ for spherical inclusions and $\eta = 1$ for cylinders with the axis perpendicular to the probing electric field). The Maxwell–Garnett theory does not consider the inclusion (ε_1) and the matrix (ε_2) in a symmetrical manner and, in fact, this model provides a reasonable estimation of the effective dielectric properties if the inclusions are not percolated and the filling factor f is smaller than about 0.3. The Bruggeman’s model takes into account the possible percolation of both components and therefore it is especially convenient for the description of the phenomena close to the percolation threshold.

As an example, bulk artificial composites for the THz range have been proposed made by deep reactive plasma etching of silicon [17, 18]; these structures can serve as more or less complex antireflective coatings [17, 19, 20] or as thick layers with on-demand refractive index (depending on the filling factor) or with high artificial birefringence [18]. An example of such a structure is shown in Fig. 22.1. Within the static approximation, it is possible to replace the structure by an equivalent electric circuit, which is shown in Fig. 22.1b. The capacitances C_x and C_y directly provide access to the effective permittivities ε_x and ε_y of the composite for the two possible polarizations of the probing electric field:

$$\begin{aligned} \varepsilon_x &= 1 + f_y \frac{f_x (\varepsilon - 1)}{\varepsilon (1 - f_x) + f_x} = n_x^2 \\ \varepsilon_y &= 1 + f_x \frac{f_y (\varepsilon - 1)}{\varepsilon (1 - f_y) + f_y} = n_y^2 \end{aligned} \quad (22.7)$$

where $\varepsilon = 11.68$ is the permittivity of silicon. The effective refractive index of the structure can be tuned between 1 and 3.4. In the case of etched silicon walls along the x -direction ($f_x = 1$) we get a highly anisotropic composite:

$$\begin{aligned} \varepsilon_x &= (1 - f_y) + f_y \varepsilon \\ \varepsilon_y &= \frac{1}{(1 - f_y) + \frac{f_y}{\varepsilon}} \end{aligned} \quad (22.8)$$

which corresponds to parallel capacitors for p -polarization (ε_x , E parallel to the walls) and to capacitors in series for s -polarization (ε_y , E perpendicular to the walls). The maximum birefringence is obtained for $f_x = 1$ and $f_y = 0.67$ and amounts as $n_x - n_y = 1.25$.

The effective medium approach can be also used for metal-dielectric composites with very small metallic particles where the conductivity (connected to the imaginary part of the permittivity) of inclusions dominates. The condition $\lambda \gg |\sqrt{\varepsilon_1}| D$ in a metal leads then essentially to the requirement that the metallic particle size is much

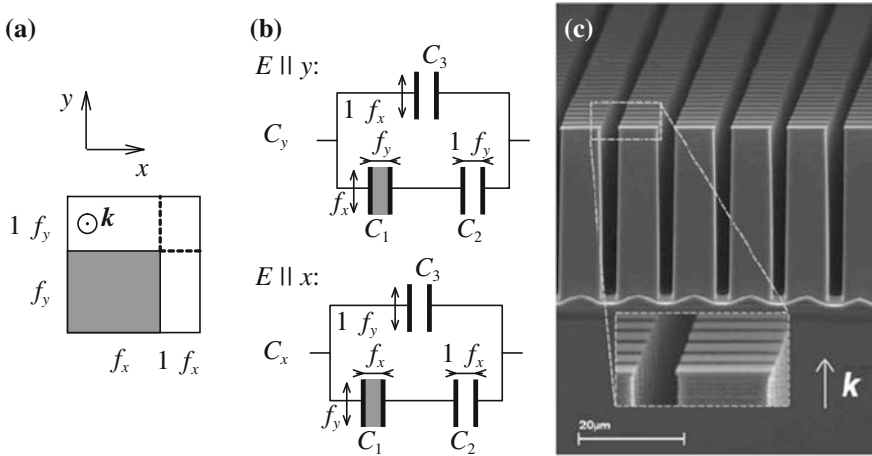


Fig. 22.1 **a** Schemes of a unit cell of an etched material with permittivity ε placed in air; the polarization of the electric field is indicated; **b** equivalent circuits for evaluating the effective response. **c** Example of etched structure: scanning electron microscope picture. After [18]

smaller than the electromagnetic skin depth. Then the details of the metal structure are too small to lead to shape-dependent resonances in the targeted spectral range (condition $\lambda \gg c\sqrt{L_{\text{int}}C_{\text{int}}}$ is satisfied, where L_{int} and C_{int} are internal inductance and capacitance of a meta-atom which are related to its shape and topology).

The response of subwavelength metallic particles is very specific and different from that of dielectric particles. This is related to the fact that the metallic conductivity inherently involves the plasmonic resonance which has a longitudinal character in a homogeneous medium (the frequency of the corresponding transverse resonance of charge carrier motion vanishes due to the lack of the restoring force). Inhomogeneities introduced in the medium then lead to the occurrence of a restoring force owing to the charge separation. In other words, the subwavelength metallic particles exhibit a high dipolar polarizability which depends on their size. The applied THz electric field then can induce charges at their edges which lead to a high effective dipole moment of the particles and a transverse plasmonic resonance may appear in the THz range in ε_{eff} [21]. Similar phenomena were also observed due to conduction-band charge carriers in photoexcited nano- or micron-sized semiconductor particles [22–24]. The plasmonic resonance is not critically dependent on the shape of meta-atoms and its existence is essentially due to the nature of metallic conductivity; for this reason it can be described by a standard EMA in analogy with the dielectrics. To illustrate the effective response of such a medium we use the Maxwell–Garnett model (22.5) considering the conductive particles, i.e.

$$\varepsilon_1 = \varepsilon_p - i \frac{\sigma_p}{\omega \varepsilon_0}, \tag{22.9}$$

where ω is the angular frequency of the radiation, ε_p is a background permittivity of the particles, and σ_p is their conductivity due to free carriers; the σ_p term is dominant in metals and its magnitude can be tuned by the excitation fluence in the photoexcited semiconductors. We assume the Drude-like behavior of the conductivity:

$$\sigma_p = \frac{\sigma_0}{1 + i\omega\tau_c}, \quad \sigma_0 = \frac{N_c e^2}{m} \tau_c, \quad (22.10)$$

where τ_c is the momentum scattering time of the carriers, m is their mass, and N_c is their concentration. Introducing (22.9) into (22.5) we find:

$$\varepsilon_{\text{eff}} = \varepsilon - i \frac{\sigma}{\omega\varepsilon_0} = \varepsilon + \varepsilon_\sigma,$$

where ε is the background permittivity of the composite which does not depend on σ_p and σ is the effective conductivity due to the metallic contribution. We find [23]:

$$\sigma = \sigma_p \frac{\varepsilon_2(1+f\eta) - \varepsilon(1-f)}{\varepsilon_2(f+\eta) + \varepsilon_p(1-f) - \frac{i\sigma_p}{\omega\varepsilon_0}(1-f)} \equiv \frac{A}{B - \frac{i\sigma_p}{\omega\varepsilon_0}(1-f)}. \quad (22.11)$$

Taking into account the Drude formula (22.10) we obtain a dielectric resonant response of the effective medium (damped harmonic oscillator formula):

$$\varepsilon_\sigma = \frac{\omega_p^2 A}{B} \frac{1}{\omega_p^2(1-f)/B - \omega^2 + i\omega/\tau_c}, \quad (22.12)$$

where the plasma frequency of the carriers in the metal is equal to $\omega_p = \sqrt{N_c e^2 / m\varepsilon_0}$. The dissipation is connected with the scattering of carriers (τ_c). The restoring force appears here due to the depolarization fields and the related separation of charges accumulated at the edges of particles; its value is related to the plasma frequency. The transverse resonant frequency:

$$\omega_0 = \frac{\omega_p}{\sqrt{\varepsilon_2 \frac{\eta+f}{1-f} + \varepsilon_p}} \quad (22.13)$$

can be tuned from 0 for $f = 1$ (homogeneous metal) up to the spectral range of ω_p for $f \rightarrow 0$.

The response of larger metallic particles may contain a magnetic contribution induced by eddy currents inside inclusions: in this case one observes a magnetic field outside the particle and the shape of the field corresponds to the magnetic dipole. It means that the effective magnetization of the composite medium can be nonzero even if the constituents are nonmagnetic. At low frequencies (the lowest order term of the power expansion in $\sqrt{\varepsilon_1 D/\lambda}$) the permeability of the spherical metallic inclusion due to eddy currents will be [25]

$$\mu_1 \approx 1 + \frac{\varepsilon_1 \omega^2 D^2}{40 c^2}. \quad (22.14)$$

We can define an effective permeability of the medium in a manner analogous to Eqs.(22.5) or (22.6) for the permittivity within Maxwell–Garnet or Bruggeman approximation, respectively (with $\mu_2 = 1$). Nevertheless, even in this case the dominant effect in the THz spectral range comes from the effective permittivity and a large number of metallic inhomogeneous systems can be described without introducing the effective magnetic properties [26]. For example, for gold spherical inclusions ($\sigma_{\text{gold}} \approx 2.1 \times 10^5 \Omega^{-1} \text{cm}^{-1}$ [27]) with a diameter of 100 nm and a filling factor $f = 0.1$ we obtain $\mu_{\text{eff}} \approx 1 - 0.004i$ at 1 THz.

22.2.3 Metamaterials

In metamaterials the electromagnetic field is inhomogeneously distributed within the fine details of the unit cell structure. The incident radiation scatters on the pattern and gives rise to the resonances which are closely connected to this inhomogeneous distribution of the local field. In principle, each scattering element is individually resonant and no interaction (interference) between the neighboring unit cells needs to be considered in order to obtain the effective resonant behavior (in practice, weak coupling between neighboring elements always exists). We deal with dielectric or metallic inclusions (scatterers) forming a motive of the structure characterized by a high permittivity or conductivity, i.e., $|\varepsilon_1| \gg |\varepsilon_2|$. The size of the individual scatterers is much smaller than the wavelength of the probing radiation in vacuum (or in the surrounding medium ε_2). This enables a procedure of homogenization of the sample, i.e., attribution of effective permeability and permittivity to the metamaterial. These effective parameters must then be able to describe the electromagnetic properties of the metamaterial from the macroscopic point of view (transmission, reflection).

A direct theoretical extension of the previous paragraph on composites is the Mie theory for fields inside and outside the spherical particles (first developed by Mie [28]). The solution of the electromagnetic field distribution inside and outside inclusions upon plane wave incidence is obtained as a multipole expansion in terms of Mie scattering coefficients which can be expressed by using spherical Bessel functions [25] for spherical inclusions or by using cylindrical Bessel functions [29] for cylindrical inclusions. In the low-frequency part of the spectra the lowest order Mie coefficients are dominating and one can develop a quasi-static extension of the Maxwell–Garnett formula for this spectral range. One obtains for spherical inclusions [30]:

$$\begin{aligned} \varepsilon_{\text{eff}} &= \varepsilon_2 \frac{1 + 3iT_1^E/u_2^3}{1 - 3iT_1^E/(2u_2^3)} \\ \mu_{\text{eff}} &= \mu_2 \frac{1 + 3iT_1^H/u_2^3}{1 - 3iT_1^H/(2u_2^3)}, \end{aligned} \quad (22.15)$$

where (T_1^E) and (T_1^H) are electric and magnetic dipole components of the scattering T -matrix of a single sphere:

$$\begin{aligned} T_1^E(\omega) &= \frac{j(u_1)[u_2 j(u_2)]' \varepsilon_1 - j(u_2)[u_1 j(u_1)]' \varepsilon_2}{h(u_2)[u_1 j(u_1)]' \varepsilon_2 - j(u_1)[u_2 h(u_2)]' \varepsilon_1}, \\ T_1^H(\omega) &= \frac{j(u_1)[u_2 j(u_2)]' - j(u_2)[u_1 j(u_1)]'}{h(u_2)[u_1 j(u_1)]' - j(u_1)[u_2 h(u_2)]'}, \end{aligned} \quad (22.16)$$

for intrinsically non-magnetic materials. Here, j and h are the spherical Bessel and Hankel functions, respectively, with the index $l = 1$, and $[xj(x)]'$ is a derivative of the expression in the square brackets with respect to the argument x . The parameters u_1 and u_2 can be understood as reduced frequencies or reduced size-parameters:

$$\begin{aligned} u_1 &= \sqrt{\varepsilon_1} \omega D / (2c) \\ u_2 &= \sqrt{\varepsilon_2} \omega D / (2c) \end{aligned} \quad (22.17)$$

It follows that the effective medium parameters in the quasistatic limit defined by (22.15) become dispersive even for a metamaterial composed of non-dispersive components. Comparing to the conditions of validity for the Metamaterial category shown in Table 22.1 we find that $u_1/\pi \approx 1$, $u_2/\pi \ll 1$. This can be achieved for high permittivity inclusions [29, 31]. It means that even if the inclusion is much smaller than the wavelength ($u_2/\pi \ll 1$), the electromagnetic field can be resonant at some frequency with a natural mode of oscillation inside the inclusion ($u_1/\pi \approx 1$). Such a condition corresponds to a pole in the scattering T -matrix; it is called the lowest order Mie resonance and it can have a magnetic or electric origin. In an analogous manner, higher multipole terms of the scattering matrix, which are not provided explicitly in this work, are at the origin of higher order Mie resonances. The resonant behavior of such structures can lead to negative ε_{eff} , μ_{eff} [31, 32] or even to the negative refractive index n [30, 33].

The spatial distribution of the near-field can be used, as originally proposed by Pendry et al. [4], for evaluation of the effective properties of the medium. The tensors of effective permittivity and permeability of the metamaterial are defined as the ratios of suitably averaged electric and magnetic displacements and fields:

$$\begin{aligned} \varepsilon_{\text{eff}}^{ij} &= \frac{\langle D_i \rangle}{\langle E_j \rangle}, \\ \mu_{\text{eff}}^{ij} &= \frac{\langle B_i \rangle}{\langle H_j \rangle}. \end{aligned} \quad (22.18)$$

where the averaging procedures were inspired by the integral form of the Maxwell equations:

$$\begin{aligned} \oint_C \mathbf{E} \cdot d\mathbf{l} &= -\frac{\partial}{\partial t} \int_S \mathbf{B} \cdot d\mathbf{S} \\ \oint_C \mathbf{H} \cdot d\mathbf{l} &= \frac{\partial}{\partial t} \int_S \mathbf{D} \cdot d\mathbf{S} \end{aligned} \quad (22.19)$$

Here, the fields are integrated over closed loops while the displacements are integrated over surfaces delimited by these contours. Thus, the macroscopic electric and magnetic fields $\langle \mathbf{E} \rangle$ and $\langle \mathbf{H} \rangle$ need to be calculated as average values along a curve. Pendry et al. [4] have proposed to average local field values along Cartesian axes of the unit cell with dimensions $a \times b \times c$ (which is chosen such that the contour does not intersect the enclosed metamaterial pattern), e.g.

$$\langle H \rangle_x = \frac{1}{a} \int_{(0,0,0)}^{(a,0,0)} \mathbf{H} \cdot d\mathbf{r}. \quad (22.20)$$

In contrast, the components of the electric and magnetic displacements \mathbf{D} and \mathbf{B} are averaged over the faces of the unit cell:

$$\langle B \rangle_x = \frac{1}{b \times c} \int_{S_{yz}} \mathbf{B} \cdot d\mathbf{S}. \quad (22.21)$$

The inhomogeneous distribution of the electromagnetic field inside the unit cell practically does not influence the average value of the fields while it strongly affects the average value of the displacement vectors. In this sense, highly inhomogeneous distribution of the near-field, reflecting a strong interaction of the radiation with the metamaterial pattern (a weak interaction would not significantly change a quasi-homogeneous character of the incident plane wave within the unit cell) may lead to high values of ϵ_{eff} and/or μ_{eff} which, in turn, describe the resonant electromagnetic behavior of the structure. This averaging procedure has been originally developed for metallic scatterers like split rings [4], but it has been successfully used also in the case of dielectric resonators [31].

With metals it is possible to deposit on a substrate planar (or even layered) structures such that their geometrical shape maximizes the electric and/or magnetic response, i.e., the charge separation (electric dipole) and the current loop (magnetic dipole). The details of the shape of such metallic inclusions then define the resonance frequency and the resonant strength. The magnetic dipole moment is related to the currents flowing along metallic rings and it can be induced if the magnetic field of the incident radiation points through the ring. The negative effective permeability was first demonstrated with split-ring resonators (SRRs) [6] and most of the experimental works in the THz spectral range published till date deal with this metamaterial structure.

22.2.4 Comparison with Photonic Crystals

As already pointed out, with metamaterials the periodicity of the structural pattern is not a requirement; each scattering element is individually resonant and the interaction between the neighboring unit cells is weak. On the other hand, if the radiation wave-

length λ becomes comparable to (or even smaller than) the characteristic distances in the structure, interferences between scattered (partially reflected and diffracted) waves become an important issue: the category of photonic crystals shown in the last column of Table 22.1 has only sense if we consider periodic structures. The condition $\lambda \approx \sqrt{\varepsilon}l$ then ensures that constructive and destructive interference phenomena may occur in the relevant frequency range for some propagation and scattering directions. This leads to the formation of the photonic band structure. From the point of view of the dispersion curves in the reciprocal space, the spectral domain where the periodic photonic structure can be described as a metamaterial remains on the lowest dispersion branch below the first band gap; the condition $\lambda \gg l$ is equivalent to $\omega/c \ll G$ (where G is the reciprocal lattice parameter of the periodic photonic structure), i.e., we deal with the wave vectors well below the Brillouin zone boundary. As the characteristic dimensions of the structure increase above $\lambda/10$ (we get closer to the Brillouin zone boundary), the homogenization of the medium may progressively become possible only if we admit the spatial dispersion (dependence of ε_{eff} and μ_{eff} on the wave vector), which is a consequence of the non-locality of the response of the structure and which is in agreement with the band structure. In a periodic medium the field distribution can be described by a Bloch wave which is a linear combination of plane waves, e.g., for the electric field:

$$\mathbf{E}(\mathbf{r}, t) = \exp(i\omega_m t) \sum_{\mathbf{G}} \mathbf{e}_{\mathbf{K}, \mathbf{G}} \exp[-i(\mathbf{K} + \mathbf{G}) \cdot \mathbf{r}], \quad (22.22)$$

where \mathbf{K} is the wave vector, m is the index of the photonic band, and the sum runs over all reciprocal lattice vectors. In the metamaterial regime a single propagative mode exists with $\mathbf{G} = 0$ within the linear combination of the above expression; the other modes are evanescent and form the near-field distribution within the metamaterial pattern. In the photonic crystal regime several propagative modes may exist which correspond to diffraction orders.

The transition between the metamaterial and photonic crystal regime was studied in the THz range by several groups [34, 35]. The authors investigated the response of single split rings in the near-field [34] and the position of the resonant frequencies as a function of the metamaterial lattice period [34] and their mutual orientation [35]. The lowest order modes are only marginally influenced by these parameters, i.e, radiative coupling between them is weak and they can be described within the metamaterial regime. On the other hand, higher order modes experience a significant spectral shift and reshaping upon a change of the parameters proving the electromagnetic coupling between the meta-atoms: this regime approaches the photonic crystal regime. The coupling between the laterally adjacent metamaterial atoms in a planar structure then depends on their density, orientation, and unit cell design [36].

22.3 Numerical Calculations and Software

Optical properties of THz metamaterials are mostly calculated using commercially available electromagnetic field simulators, which permit straightforward numerical simulations of almost arbitrary complex structures with quite versatile boundary conditions. These programs typically employ some of the well-known methods [37] for a numerical solution of Maxwell's equations (22.4). For example, the Ansoft HFSS utilizes a finite-element method and optionally, the method of moments is also implemented [38]. The CST Microwave Studio solvers use either a finite-difference time-domain algorithm, or a finite integration technique [39]. Unfortunately, we did not find in the literature any comparison in terms of accuracy or calculation speed of these approaches applied to simulations of THz metamaterials. Other numerical methods are used only seldom and in rather specific cases. Among them, transfer matrix method is suitable for simulations of periodic metamaterials [31, 40–43]. Rigorous coupled-wave analysis can be employed for the investigation of planar gratings [44, 45].

22.4 Experimental Characterization

In the THz spectral range two experimental methods are mainly employed for a broadband characterization of metamaterials: Fourier-transform infrared spectroscopy (FTIR), and time-domain THz spectroscopy (TDTS). Both methods provide access to transmittance and reflectance spectra. FTIR is typically used for the measurement of the power (intensity) spectra, whereas TDTS enables simultaneous characterization of the amplitude and phase in the THz spectral range.

We will discuss various approaches reported in the literature, each of them providing a different amount of information about the electromagnetic response of metamaterials. The measured power or amplitude spectra can reveal the existence of resonances and their spectral positions and strengths, but they provide only little insight into their nature. An agreement between the measured and calculated power spectra of the investigated structure is frequently considered as a proof of the targeted metamaterials properties [46–48]. A somewhat extended view can be obtained by measuring spectra at different sample orientations, polarizations of the incident light, and angles of incidence; in this way it is possible to distinguish between electric and magnetic resonances [49, 50]. A detailed picture can be gained by a retrieval of effective optical properties from the measured spectra. The results are able to bring direct proofs of negative effective refractive index or, e.g., negative effective magnetic permeability [31, 50–52]. This advantage is paid by a high level of sophistication of the experimental methods required for unambiguous characterization of metamaterials exhibiting both effective dielectric and effective magnetic response in the same spectral range. Finally, an ultimate amount of information comparable to that available from numerical simulations can be obtained from the measurement

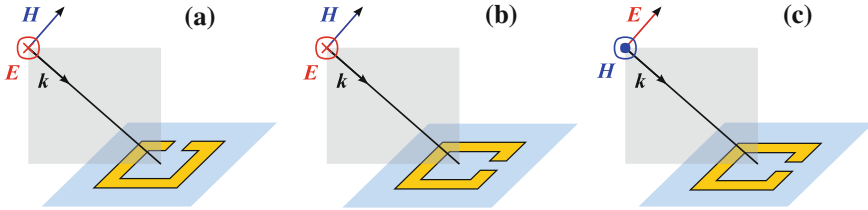


Fig. 22.2 Geometries employed for investigation of split-ring-based metamaterials; the gray surface indicates the incidence plane. **a** s -polarized incident beam with in-plane electric field of the mirror symmetry of the metamaterial excites the magnetic resonance solely by the magnetic field. **b** s -polarized light with out-of-plane electric field of the mirror symmetry of the metamaterial enables a coupling of the magnetic resonance to the incident electric field. **c** p -polarized light does not allow exciting the magnetic resonance

of distribution of electromagnetic fields within the metamaterial structure by using near-field THz imaging techniques [34, 53].

22.4.1 Electric and Magnetic Resonances

Most THz metamaterials targeted to exhibit a magnetic resonance are based on SRRs. Their magnetic response originates from circular currents induced in the split rings. The magnetic resonance can be excited magnetically, when the incident magnetic field has a component perpendicular to the plane of the SRR [4], Fig. 22.2a,b. In structures composed of just limited number of layers of split rings, this requires an oblique incidence of the probing radiation. Alternatively, the magnetic resonance can be excited electrically, when the structure does not show the mirror symmetry with respect to the incident electric field [49].

These simple arguments made it possible to assess the nature of the response for the first THz metamaterials based on SRRs. Yen et al investigated a THz metamaterial composed of double SRRs by FTIR spectroscopy [7]. The light irradiated the sample at 60° from the normal. In this configuration, only the s -polarized light may excite the magnetic resonance at ~ 1 THz whereas no magnetic response is expected for the p -polarized light. This behavior was confirmed by the measurement of the reflectance ratio $|r_s/r_p|^2$ (r_s and r_p are complex reflectances for the s - and p -polarized light, respectively) which shows a broad peak at the spectral position of the magnetic resonance of the metamaterial [7]. Driscoll et al. studied a structure composed of symmetrized pairs of SRRs where the coupling of the electric field to the magnetic resonance is suppressed [50], see inset of Fig. 22.3a. The increase of the angle of incidence of an s -polarized light from the normal to 45° then leads to a clear appearance of a resonance which can be reliably associated with a magnetic response (Fig. 22.3a).

The difference between electric and magnetic excitation of the magnetic resonance was experimentally studied by Gundogdu et al. in an array of single SRRs with a magnetic resonance predicted at ~ 6 THz [49]. The metamaterial was irradiated with an s -polarized light, the angle of incidence was varied, and two different orientations of the metamaterial were used. When the split rings possess the mirror symmetry with respect to the electric field vector, the electric field cannot couple to the magnetic resonance. The component of the magnetic field which couples to the magnetic resonance then increases with increasing angle of incidence; this results in the observed increase of the resonance strength (Fig. 22.3b). When the metamaterial is rotated by 90° , the electric field can couple to the magnetic dipole and a strong resonance almost independent of the angle of incidence appears in the optical spectra (Fig. 22.3c).

Most of the studied metamaterials possess a mirror-plane symmetry containing the direction of propagation. Their eigenstates are linearly polarized waves [54]. However, there have been also several efforts to manipulate the polarization state of the light by using chiral metamaterials. Characterization of such metamaterials then involves determination of the ellipticity and the azimuth of transmission or reflection eigenstates [55].

22.4.2 Retrieval of Effective Properties

A detailed insight into the properties of metamaterials can be gained through the determination of their effective optical properties such as effective refractive index and wave impedance or effective magnetic permeability and dielectric permittivity. These properties can be in principle obtained when both complex transmittance (t) and complex reflectance (r) spectra are measured. For normal incidence the transmittance and reflectance spectra read as [43, 56]:

$$\begin{aligned} t &= \frac{1}{\cos(\omega Nd/c) + \frac{i}{2}(Z + Z^{-1}) \sin(\omega Nd/c)} \\ r &= \frac{i}{2}(Z - Z^{-1}) \sin(\omega Nd/c) t \end{aligned} \quad (22.23)$$

where d is the sample thickness, ω is the angular frequency, c is the speed of light in vacuum, N is the complex (effective) refractive index, and Z is the complex relative (effective) wave impedance of the metamaterial. The complex permittivity and permeability are then related to N and Z :

$$\begin{aligned} \mu &= NZ \\ \varepsilon &= N/Z \end{aligned} \quad (22.24)$$

Note that the expressions in (22.23) are complex conjugates to the original ones reported in [43]; this is owing to our convention of the complex formalism.

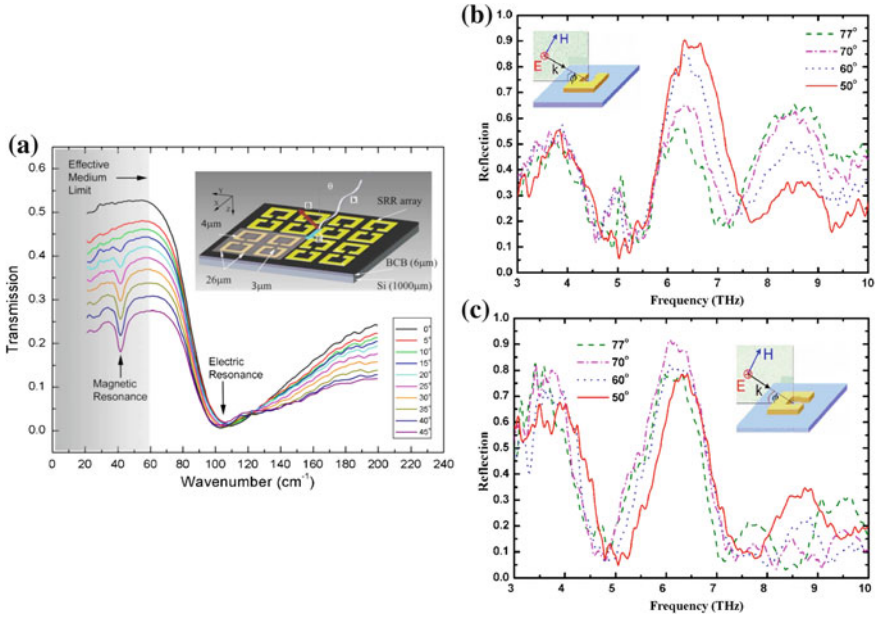


Fig. 22.3 **a** Transmittance spectra of a symmetrized array of single SRRs measured by an *s*-polarized light for various angles of incidence. A narrow magnetic resonance appears for nonzero angle of incidence when a magnetic field component perpendicular to the split-ring surface induces circular currents in the split rings. There is also a much stronger electric resonance almost independent of the angle of incidence. After [50]. **b**, **c**. Reflectance spectra measured by *s*-polarized light in an array of single SRRs. The spectra exhibit a magnetically **b** and electrically **c** excited magnetic resonance around 6 THz. After [49]

These equations can be straightforwardly inverted, yielding

$$Z = \sqrt{\frac{(1+r)^2 - t^2}{(1-r)^2 - t^2}} \tag{22.25}$$

$$N = \frac{c}{\omega d} \arccos \left[\frac{1 - r^2 + t^2}{2t} \right]$$

The transmission function t relates the output electric field to the input one: $t = E_{\text{out}}/E_{\text{in}}$. In spectroscopy, a reference measurement is frequently performed without the sample in the beam path; the transmission function in this case is equal to the phase change due to the propagation in vacuum: $t_0 = \exp(-i\omega d/c)$. The spectroscopic transmittance is then usually defined as a relative one with respect to the reference $t' = t/t_0$. In a similar manner the spectroscopic reflectance is defined with respect to some reference reflection measurement r_0 : $r' = r/r_0$ (for a perfect metal mirror $r_0 = -1$).

There are several theoretical and experimental challenges. First of all, as already discussed, the homogenization limit for the metamaterials is typically set as $D < \lambda/10$. However, a considerable activity in the research of electromagnetic metamaterials has been devoted to structures above this limit ($> \lambda/10$). This implies a non-negligible spatial dispersion of the effective optical parameters observed when the light propagation direction is varied. At the same time the discontinuous nature of the metamaterial leads to ambiguities in the retrieved parameters. This is essentially related to the reflectance phase. The exact position of the input and output faces of the metamaterial is not defined and the uncertainty is comparable to the period l of the pattern in the direction perpendicular to the surface ($> \lambda/10$). From the practical point of view, it is not clear where to position a mirror for the reference measurement: the phase of the reflectance is ambiguous within $\sim i\omega l/c$. If the metamaterial does not contain a mirror plane perpendicular to the propagation direction, the metamaterial reflectance and, in turn, also the retrieved effective optical properties in principle depend on from which side of the metamaterial the reflectance is measured. At least for metamaterials periodic in the propagation direction, it is possible to evaluate the phase shift introduced by a single period, which enables rigorous definition of the refractive index [56].

Metamaterial test samples for the THz range and for higher frequencies often consist of a single patterned plane (single-layer metamaterials) with the physical thickness much smaller than the probing wavelength. The problem here is 2-fold. We can ask an analogous question on the atomic level: is it reasonable at all to define ε and μ for the description of the electromagnetic response of a single atomic layer and will these functions still correctly describe the response if a bulk sample is grown? In the metamaterial science, we have an additional degree of freedom: the possibility to choose the period of the pattern. In order to assign a meaningful effective bulk permittivity and permeability to a thin film metamaterial from the spectroscopic results a convenient effective thickness d_{eff} should be chosen. For example, this thickness may be understood as a decay length of the local fields out of the metamaterial plane [57]. This brings a large ambiguity to the effective parameter retrieval procedure both from the point of view of the reflectance phase (as pointed out above) and from the point of view of the choice of d_{eff} . At the same time this approach of the estimation of bulk effective parameters from a thin film can be only valid if the targeted bulk metamaterial has an out-of-plane period close to d_{eff} . One intuitively feels that, for example, for a period of the layer stacking smaller than d_{eff} , the interaction between the metamaterial planes will significantly influence the near-field pattern and modify the effective response of the bulk sample.

Finally, there are technical complications associated with the multivalency of the square root and arccos functions. The condition of the passivity of the metamaterial leads to a certain disambiguation of (22.25), since it implies $\text{Re } Z > 0$ and $\text{Im } N > 0$. However, the solution for the refractive index contains several branches originating from the arccos function. In some cases it may be difficult to select the right one; this is particularly true for thick samples, for which the branches are closely spaced.

From the experimental point of view, it is difficult to obtain the phase information at high frequencies. Nevertheless, in the THz range the phase can be still measured by

means of TDTS. The transmittance phase can be generally measured very accurately and its precision is limited only by the accuracy of delay stages. Measurement of the reflectance phase is complicated since when the sample is replaced by a reference mirror, a longitudinal offset resulting in a substantial phase shift may be introduced. It is necessary to take extreme precautions to eliminate this shift, since even micrometer offsets may cause a significant error in optical parameters retrieved from optical spectra [58].

Minowa et al. [51] measured complex reflectance and complex transmittance spectra of phosphor bronze wire grid by TDTS. Due to a tens-of-microns displacement of the sample with respect to the reference mirror in the reflectance measurements, the reflectance phase had to be optimized numerically during the retrieval of the effective optical properties. The results then confirmed that the effective permittivity of the wire grid shows a plasmonic resonance in the THz region for electric field parallel to the wires [2] and that the effective permittivity is positive for electric field perpendicular to the wires. Awad et al. [52] investigated a metamaterial made of H-shaped wire-pair resonant structures which were designed to exhibit a range with negative refractive index. The negative refractive index was confirmed experimentally, but no details about its retrieval from the experimental data were provided [52].

An approach avoiding the difficulties connected with the measurements of the reflectance spectra consists in a measurement of amplitude transmittance at several incidence angles. This approach was used by Driscoll et al. for the characterization of an array of SRRs by FTIR spectroscopy [50, 57]. However, a full inversion of the equations connecting the transmitted power to N and Z was not performed; instead, the magnetic response was modeled by a modified Lorentzian function and only its parameters were retrieved by fitting the experimental data [50].

22.4.3 Retrieval of N and Z from Time-Windowed Signal

TDTS consists in measuring the temporal profile of the electric field of a broadband THz pulse transmitted or reflected by a sample. The multiple internal reflections of the THz pulse in an optically thick sample are measured as a series of mutually delayed echoes in the time domain (Fig. 22.4b).

$$\begin{aligned} t' &= \sum_{i=0}^{\infty} t'_i \\ r' &= \sum_{i=0}^{\infty} r'_i \end{aligned} \tag{22.26}$$

The temporal windowing can be then applied to such data in order to separate the signals belonging to these echoes [59] and calculate the transmission or reflection functions t'_i, r'_i for these partial waves. In order to obtain two complex spectroscopic quantities allowing one to determine N and Z (or ε and μ) it is then sufficient to consider two of such measured transmittance or reflectance signals. The methods of extraction of N and Z from these quantities without any ad hoc assumption about the behavior of ε and μ were described in [60], where the lowest order transmittance

and reflectance functions t'_0 , t'_1 , and r'_0 were considered. For normal incidence one obtains:

$$\begin{aligned} t'_0 &= \frac{4Z}{(Z+1)^2} \exp[-i\omega(N-1)d/c] \\ t'_1 &= t_0 \left(\frac{Z-1}{Z+1} \right)^2 \exp(-2i\omega Nd/c) \\ r'_0 &= \frac{Z-1}{Z+1} \end{aligned} \quad (22.27)$$

A thorough analysis of the sensitivity of these retrieval methods and of their experimental errors was also presented in [60]. These methods allow a quite accurate determination of N while the error in the determination of Z is usually significantly higher: successful evaluation of the dielectric and magnetic dispersion then crucially depends on the accuracy of the wave impedance measurements.

As pointed out above the metamaterial samples are frequently very thin and in this case the separation of echoes in the time domain is impossible. For this reason it was proposed to attach the metamaterial in an optical contact to a thick transparent substrate and analyze the echoes coming from the reflection on a backside of the substrate (see Fig. 22.4). A metamaterial consisting of a grid of high-permittivity rods made of paraelectric SrTiO₃ (Fig. 22.5a) has been characterized by using this approach by Němec et al. [31]. For an incident wave with electric field perpendicular to the dielectric rods, the metamaterial should exhibit a magnetic response and a negative effective magnetic permeability associated with the lowest order Mie resonance [29, 31]. The metamaterial was attached to a 2 mm thick silicon wafer, which made it possible to temporally resolve the internal reflections in the substrate. The substrate without the metamaterial sample attached then served for the reference measurement. The metamaterial reflectance and transmittance read as

$$\begin{aligned} t' &= \frac{E_{\text{sam}}^{(0)}}{E_{\text{ref}}^{(0)}} \\ r' &= \frac{E_{\text{sam}}^{(1)}}{E_{\text{ref}}^{(1)}} \cdot \frac{r_s}{t'} \end{aligned} \quad (22.28)$$

where $r_s = (N_s - 1)/(N_s + 1)$ is the reflectance on the substrate–air interface and N_s is the (possibly complex) refractive index of the substrate (see Fig. 22.4). Note that the large phase shifts induced by the substrate exactly cancel out, as identical substrates are used in both measurements. The reflectance phase is thus free of systematic errors due to possible mispositioning of the reference (a good contact between the metamaterial and the substrate is required). The retrieved effective permeability shows a strong resonance at 0.264 THz and a region with negative effective permeability above this resonance (Fig. 22.5c). Two weaker magnetic resonances originating from higher order Mie-modes are observed at ~ 0.53 THz and 0.61 THz. The response is not purely magnetic as weak resonances are clearly observed also in the permittivity.

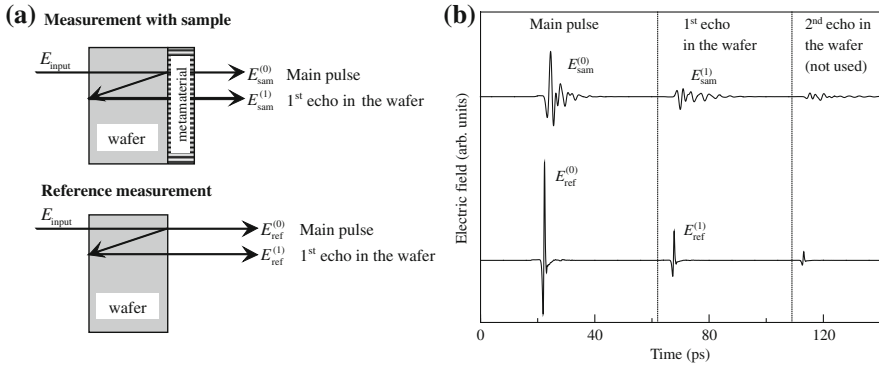


Fig. 22.4 **a** Scheme of the arrangement for transmittance and reflectance measurement in TDTS, along with a sketch of the required reference signals. The THz beam is shifted upon reflections only for graphical clarity. **b** Illustration of a typical waveform obtained in TDTS

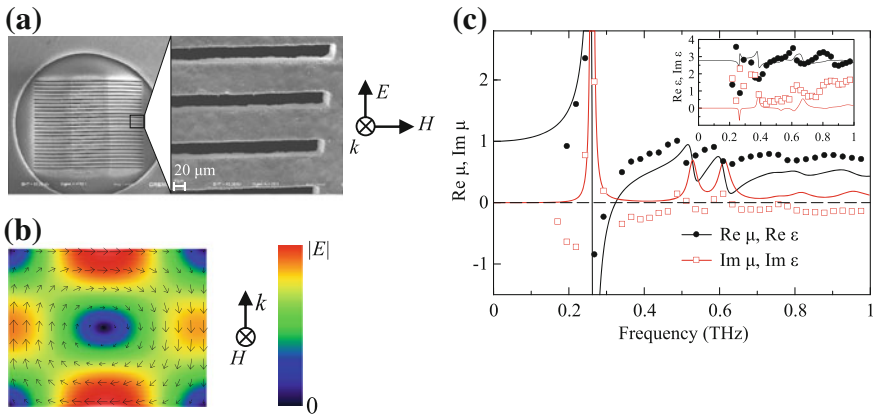


Fig. 22.5 **a** Scanning electron microscopy image of an array of SrTiO₃ rods. **b** Distribution of the electric field in a rod at the lowest order magnetic resonance frequency. The circular current is responsible for the magnetic response. **c** Effective magnetic permeability and dielectric permittivity spectra. Symbols: measurement, lines: calculations by multidimensional transfer matrix method

The spectral resolution of this method is imposed by the time-windowing and it is then essentially determined by the substrate thickness. In [31] a 2 mm thick Si wafer was used which limited the frequency resolution to ~ 22 GHz and led to a broadening of the observed resonance in μ_{eff} .

It should be noted that the measurements can be greatly simplified for composites or for metamaterials with a symmetry which does not allow the magnetic response. The magnetic permeability is then equal to 1 and the resonant permittivity can be retrieved simply from complex transmittance measurements by well-established standard methods of TDTS [18, 61, 62].

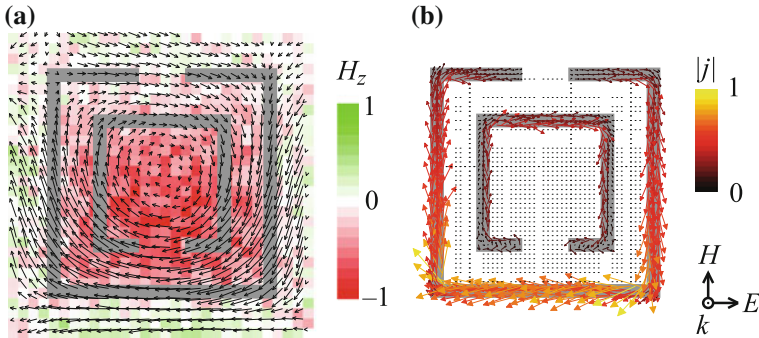


Fig. 22.6 **a** Measured electromagnetic near-field distribution close to a double SRR at a resonance frequency denoted as A1 in Ref. [53]. The vector plots show the in-plane electric field vectors in the x - y -plane at the backside of the sample. The color code indicates the time derivative of the out-of-plane component of the corresponding magnetic field, $\partial H_z/\partial t$, derived from the electric field vectors. **b** Simulated surface current density. After [53]

22.4.4 Near-Field Methods

An ultimate experimental technique which can facilitate understanding of the metamaterial physics and provide an amount of information comparable to that obtained from numerical simulations is the near-field THz imaging. Bitzer et al. [34] developed a TDS equipped with a THz detector based on an antenna with a $10\ \mu\text{m}$ wide gap between H-shaped electrodes on an ion-implanted silicon-on-sapphire substrate. By scanning the position of the detector chip across the metamaterial, they obtained a two-dimensional (2D) map of the electric field components in the metamaterial plane with a subwavelength spatial resolution. From Maxwell's equations, it is then possible to reconstruct even the spatial profile of the magnetic field perpendicular to the metamaterial plane [53]. The near-field imaging technique was used to investigate the field distribution at a resonant frequency in an array of double SRRs [53]. The result of such a measurement along with the calculated current density distribution in the split ring is illustrated in Fig. 22.6 for the case of the lowest magnetic resonance. The plots show the eddy currents leading to the magnetic response, and the induced magnetic field inside the split rings.

Finally, let us mention the work by Seo et al. who employed near-field imaging for investigation of a slit array in a metal foil [63]. In this work, two electro-optic crystals sensitive to different components of the electric field were alternatively used as detectors. This allows a full characterization of the electric field vector, which in turn enables evaluation of all derived quantities such as Poynting vector or all components of the magnetic field vector.

22.5 Fabrication of THz Metamaterials

Many THz metamaterials are prepared in the form of patterned layered structures which makes the fabrication easier compared to 3D metamaterials. Planar metamaterials can be straightforwardly machined by lithography or by direct laser writing. Both these techniques can be combined with further micromachining steps to prepare more sophisticated structures.

22.5.1 Lithography

Typical dimensions of metallic resonators in THz metamaterials are of the order of tens of micrometers and the smallest details of the metallic patterns then reach units of microns. This predestinates the optical or UV lithography followed by a lift-off process as a routine technique for the fabrication of planar THz metamaterials. Indeed, many THz metamaterials have been fabricated by this method, e.g., [7, 8, 47, 49, 50, 64, 65] to cite just a few early papers dealing with THz metamaterials. The technology was further enhanced to fabricate more complex structures. Yen et al. employed a self-aligned technique called a photo-proliferation process to produce thick metallic patterning of a double-SRR array with a period $\sim 30\text{--}50\ \mu\text{m}$ which exhibits a magnetic resonance near 1 THz [7], Fig. 22.7a. The first layer of the pattern was prepared by optical lithography in a standard way. In the second step the exposure was performed from the back side of the sample and the primary metallic pattern served as the mask. This approach allows depositing thick metallic structures while avoiding alignment problems. In the work by Katsarakis et al. [47], the authors repeated the UV lithography process several times in a layer-by-layer fashion to build a negative-permeability metamaterial consisting of five aligned metallic layers of SRRs (mutually isolated by polyimide layers) with the alignment accuracy of $0.5\ \mu\text{m}$ ensured by a commercially available aligner. These resonators were arranged in a square lattice with a period of $7\ \mu\text{m}$, and the operating frequency was around 6 THz.

Chen et al. performed two lithographical steps to deposit an ohmic electrode and interconnected resonators [8, 66, 67], (Fig. 22.9). The final metamaterial array and the doped semiconductor substrate form together a Schottky diode. Wu et al. employed a UV stereo-microlithography for the fabrication of an array of vertical rods ($30\ \mu\text{m}$ diameter, 1 mm height) [68]. Their stereo-microlithographical system contained a beam-shaping element delivering a mask pattern to the projection lens, which focused the UV light onto the surface of the resin. Under the exposure, a thin layer of solid polymer structure was formed by the computer generated mask pattern according to the sliced cross-section of the digital 3D model. By stacking the layers sequentially in the course of lowering the elevator, a solid polymer copy was fabricated of the liquid resin according to the digital 3D model. After coating of the

rods array by a metal, the structure served as a plasmonic high pass filter with cutoff frequency of 0.7 THz.

Optical lithography was also used to fabricate planar arrays of 50- μm SRRs on bimaterial cantilevers designed to bend out-of-plane in response to a thermal stimulus [69], Fig. 22.7b. This resulted in a controlled response of the electric and magnetic resonance (~ 0.5 THz) as the SRRs reorient within their unit cells.

From the point of view of potential applications, it is important that optical lithography can manufacture even flexible THz metamaterials [70–74].

The spatial resolution in optical lithography is limited by the wavelength of the employed light source. One advantage of shorter wavelength sources is the possibility to deliver nearly vertical sidewalls. This opportunity was utilized by Moser et al who used X-ray lithography to form a free-standing THz metamaterial with a negative refractive index at Fig. 22.7c. Deep X-ray lithography was used for the production of stacked split ring structures resonant around 5 THz to obtain a larger height of the pattern (dimension perpendicular to the lithography plane) in order to reduce the anisotropy [76]. A good spatial resolution is particularly important for metamaterials targeted for higher frequencies, since they involve smaller motives. Electron beam lithography was thus successfully used for the preparation of SRRs with magnetic resonance in the mid-infrared spectral region [77]. Chen et al. combined the electron beam lithography for the deposition of metallic patterns with the optical lithography followed by a reactive ion etching of a thin silicon layer: the resulting structure contained 50- μm -sized metallic resonators connected to small silicon capacitor-like structures [78]; the silicon pads were excited optically during the THz experiments in order to switch the metamaterial resonant frequency (see Fig. 22.12 and the corresponding text).

Lithographical techniques can be efficiently combined with deep etching procedures, typically to produce vertical semiconducting rods. Kadlec et al. [18] prepared a metallic mask using an optical lithography, and subsequently employed an anisotropic deep inductive plasma etching to produce silicon pillars or walls with characteristic lateral dimensions below 10 μm and with a up to 80 μm , Fig. 22.1c. Such layers can exhibit an on-demand refractive index determined by the geometrical parameters of the structure. Similarly, Bruckner et al. [17] prepared a mask by an electron-beam lithography and performed a deep etching to produce an array of 500 μm high silicon pillars with a lateral dimension of ~ 40 μm ; these played the role of a broadband antireflection coating. Finally, Saha et al. [79] imprinted a similarly fabricated rigid-wall structure on both sides of a high-density polyethylene. Such a structure with 60- μm period then acted as a quarter-wave plate operating between 2.6 and 3.8 THz, depending on the depth of the imprint.

22.5.2 Laser Writing

Direct laser writing is quite a versatile process. In the early times, a double-split-ring structure combined with cut wires was fabricated by direct laser writing comple-

mented by electroplating [80]. The fabricated 100- μm resonators exhibited a pass-band around 2 THz, which was attributed to the negative refractive index. Direct laser writing was also used for the elaboration of various planar metallic microresonators with electric resonant response on a flexible polyimide substrate [71]. With a characteristic period of about 50 μm , they exhibited a resonance in the THz range. Direct laser writing can be used to obtain even tinier patterns with resonances reaching the mid-infrared region. Moreover, the fabrication of 3D structures is also possible. These capabilities were combined by Rill et al. [81] to develop a negative-index metamaterial with a resonance at around 100 THz corresponding to the pattern period of 1 μm .

Direct writing by proton beam is suitable for cutting strictly vertical structures as the large mass of the protons allows them to maintain straight tracks through many microns of the resist. By using an additional electroplating step, Chiam et al. produced high narrow metallic structures, Fig. 22.7i. The resulting array of split rings enclosed by 40- μm closed square rings exhibited similarities with electromagnetically induced transparency, such as a large group index and low losses for frequencies around 1.25 THz.

22.5.3 Other Techniques

Laser cutting is a promising technique with the potential to micromachine a wide variety of materials. In Ref. [31, 83], an array of 30- μm grooves was drilled by a femtosecond laser into 20–50 μm thick SrTiO_3 wafers. The resulting array of high-permittivity rods exhibited a strong Mie resonance accompanied by a negative effective magnetic permeability (Fig. 22.5). Micromachining was also used for cutting an array of 100- μm -sized SRRs [84].

Various efforts have been made to reduce the costs and to achieve a greater versatility of the fabrication process of THz metamaterials. Early attempts demonstrated the possibility to prepare simple structures like THz wire-grid polarizers by ink-jet printing [85, 86]. Walther et al. [87] employed an ink containing a suspension of silver nanoparticles and printed an array of SRRs on a flexible kapton foil, Fig. 22.7e. Due to their large dimensions (0.5 mm), they were targeted rather for sub-THz frequencies. Ink-jet printed cut wires were prepared by Takano et al. to study an insulator-to-metal transition [88]. Another direction is devoted to the possibility to fabricate THz metamaterials by self-organization. Pawlak et al. [89] investigated a directional solidification of eutectics which leads to a realization of self-organized particles with an SRR-like cross section, Fig. 22.7f.

The above list of techniques is far from exhaustive – below we provide a few examples which go beyond the above classification. Hollow staple nanostructures resembling 3D Ω -shaped metallic nanostripes were designed and produced by Zhang et al. [90] exhibiting a negative effective permeability at tens-THz frequencies, Fig. 22.7d. Tuniz et al. [91] presented a metamaterial acting both as a polarizer and as a high-pass filter: it was based on a fiber drawing where a macroscopically sized

(\varnothing 1 cm) preformed metal-dielectric fiber was heated and reduced in size (below 1 mm diameter) which produced the desired size of the patterns. The output fiber then contained $\sim 100 \mu\text{m}$ spaced metallic fibers with a diameter of $8 \mu\text{m}$. Miyamaru et al. employed laser processing to deposit a large number of metamaterial layers and assembled them together to obtain a bulk magnetically active metamaterial [92, 93] – the resonant frequency of 0.35 THz was achieved with 100- μm SRRs. Wen et al. [94] employed plasma etching to prepare a metamaterial composed of cut VO_2 wires. VO_2 exhibits a metal-to-insulator transition which predestines the use of such a metamaterial for thermally controlled switches. Crystallographic wet etching was employed by Chen et al. [95] to develop a broadband antireflection coating made of tens-microns-sized pyramids formed in a silicon wafer by crystallographic wet etching, Fig. 22.7g. Notable is also a negative-refractive-index chiral metamaterial by Zhang et al. which contains planar metallic wires (= capacitors) connected by 3D metallic bridges (= inductances) [96], Fig. 22.7h. Wire-cut electrical discharge machining was employed to develop a metamaterial with high effective refractive index based on a metallic grating [97].

22.6 Applications

Several principal research directions in the THz metamaterials can be traced from the published literature. (i) The first one is the search for structures with negative refractive index, which was historically the first motivation for the metamaterial development. As it is in principle much easier to find or to design a sample with a negative permittivity, the authors deal mainly with the problem of how to obtain the negative permeability. (ii) Another class of papers is devoted to the application where the authors look for the way to tune or modulate the metamaterial resonance. In a number of works the accent is put on structures where the magnetic response is forbidden by the symmetry and the metamaterials exhibit an artificial dielectric resonance controlled by an external parameter like electric field or fotoexcitation. In this sense, here we deal with the search for the tunability by means of metamaterial structures. (iii) The plasmonics is a modern topic of research aiming at applications in the development of chemical and biochemical sensors and which can help to miniaturize various optical components. A number of papers on research in the field of THz plasmonics with metamaterials have been published [98–101]—we will not discuss the THz plasmonics here as a separate chapter of this book is devoted to the advances in this topic. (iv) The strong interaction of light with metamaterial structures allows one to conceive metamaterial-based absorbers, (v) artificial birefringence of anisotropic metamaterials allows one to achieve the metamaterial-based polarimetry and finally, (vi) some specific effects like cloaking, waveguiding, or achieving “slow-light” effects with metamaterials have also been reported.

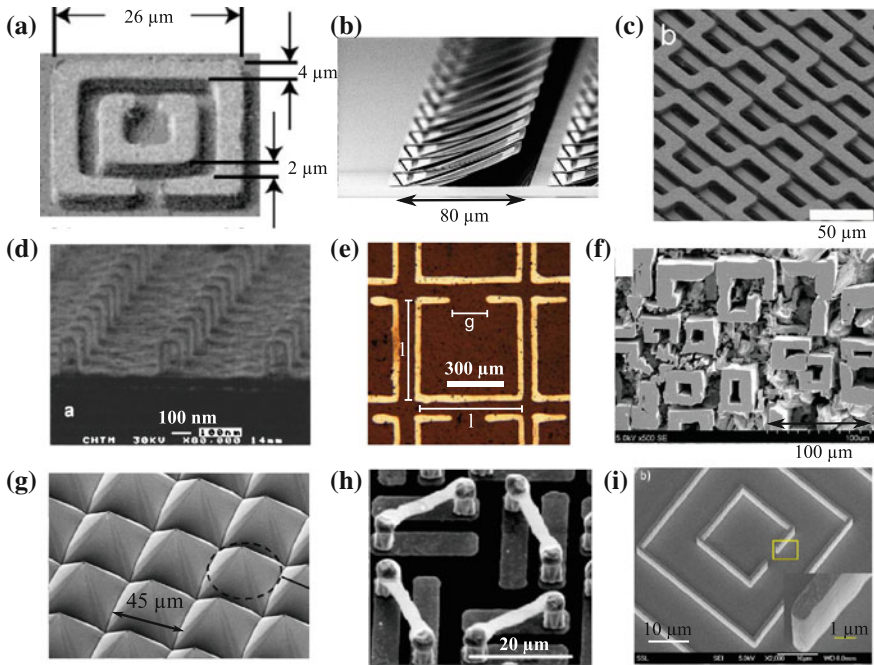


Fig. 22.7 A few examples of THz metamaterial structures. **a** A secondary ion image of a double-split ring taken by focus ion-beam microscopy, after [7]. **b** SEM picture of SRRs on bimaterial cantilevers, after [69]. **c** SEM image of double-S metamaterial, after [75]. **d** Omega-like metallic nano-strips, after [90]. **e** Ink-jet printed split rings, after [87]. **f** SEM image of a split-ring-like structure grown from SrTiO₃-TiO₂ eutectics and covered by metal, after [89]. **g** SEM image of silicon micropyramids, after [95]. **h** SEM image of a chiral material, after [96]. **i** SEM image of a metallic resonator fabricated by proton writing. The height of the resonator is 4 μm. After [82]

22.6.1 Negative Permeability

The majority of structures aiming at the negative μ are based on the split-ring resonators (SRRs). These can have various shapes, e.g., circular or square double-SRRs as shown papers [6, 7] (see Fig. 22.7a) or single SRRs or single SRRs [47, 50, 87], (see Fig. 22.7e). The magnetic dipole moment is related to the currents flowing along metallic rings and the disadvantage of these structures is that the effective magnetic response can be induced only for an oblique incidence of the radiation when the magnetic field points through the ring as shown in Fig. 22.2a, b. Various approaches have been proposed and explored to overcome this problem.

Recently, Miyamaru et al. stacked together 100 layers of 2D dielectric sheets patterned with SRRs and obtained a bulk piece of metamaterial with a thickness of 10 mm [102]. This allowed performing experiments with the incident wave vector lying in the split-ring plane; in this geometry either the magnetic or the electric field is perpendicular to the plane of the SRRs. In agreement with theoretical predictions

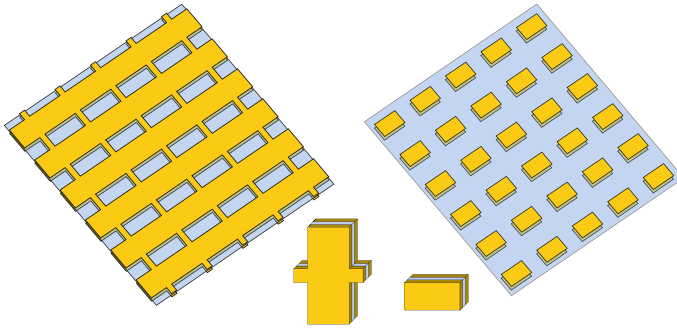


Fig. 22.8 Fishnet (*left panel*) and cut-wire pair (*right panel*) structures consisting of metallic double layer (*yellow*) separated by a thin dielectric material (*blue*). The negative permittivity and permeability can be achieved here for a normal incidence of the radiation [105]

[4, 6] the electric field perpendicular to the plane of the SRRs does not lead to any resonant response, whereas for magnetic field perpendicular to the plane of the SRRs, a strong narrow magnetic mode and a broader weaker electric mode (resulting from the half-wavelength electric dipole resonance of one side of the SRR) are observed.

Another solution has been proposed by Fan et al. who developed a layer of 3D stand-up metamaterials prepared by multilayer-electroplating technique consisting of out-of-plane SRRs standing upon the substrate [103, 104]. For the normal incidence the magnetic-field vector perpendicular to the SRR plane induces circular currents in the rings and a strong magnetic response appears. A similar idea on a more elaborated basis has been demonstrated by the same group with so-called reconfigurable THz metamaterials [69], see Fig. 22.7b.

Other possibilities to create magnetically active metamaterials take advantage of the displacement currents in dielectrics which can form parts of the current loops. Various kinds of structures composed of finite length (cut) wire pairs or with the fishnet double-layer topology were developed [105, 106]. The currents flow here through the metallic parts but the displacement currents between the two adjacent layers with deposited cut wires or fishnets (which are separated by a thin dielectric) allow one to obtain closed current loops and to achieve a resonant magnetic response even for the normal incidence, see Fig. 22.8.

The Mie resonances of dielectric inclusions provide another interesting mechanism for the creation of magnetic resonances based entirely on displacement currents, and even offer a versatile route for the fabrication of isotropic metamaterials operating at THz frequencies. In these structures, ferroelectric or polaritonic compounds with high permittivity can be typically used and also their tunable behavior presents an advantage in designing commandable structures [107–109].

The discussed phenomena were first demonstrated in a ferroelectric $(\text{Ba,Sr})\text{TiO}_3$ ceramics in the GHz frequency range [32]. In the THz range thermally tunable magnetic Mie resonances were obtained in an array of SrTiO_3 rods for the *s*-polarized THz beam, i.e., E perpendicular to the rods (Fig. 22.5a). The resonant behavior is

closely connected to the high value of the permittivity in SrTiO₃ (~ 300 at room temperature and ~ 1200 at 100 K in the sub-THz range [110]). The resonant behavior can be understood with simple physical arguments: the wave front of an incident plane electromagnetic wave undergoes a strong distortion close to the metamaterial in order to satisfy simultaneously the continuity and discontinuity conditions of tangential and normal electric-field components at the SrTiO₃–air interfaces, respectively. The electric field, which develops inside an SrTiO₃ bar, is then predominantly tangential close to the surface of the bar. This leads to the creation of displacive eddy currents within the bar cross-section (Fig. 22.5b) which enhance the magnetic field in SrTiO₃ polarized along the bar. A resonant behavior is then expected at specific frequencies determined by the geometry and dielectric constants of the rods (Fig. 22.5c). The effective properties of the metamaterials were thermally tuned over a broad spectral range owing to the dielectric tunability of the SrTiO₃ crystal [31].

22.6.2 Tunable Metamaterials

In the metamaterial science the THz technology serves, on the one hand, as a platform for extension of GHz-scaled structures up to the optical range. On the other hand, properly designed structures utilizing specific THz material properties allow one to create metamaterial devices targeted for THz applications. It is expected that many of these applications will require manipulation of the flow of THz radiation either passively (waveguides, splitters) or actively by a variation of an external parameter (modulators, switches, tunable filters). At the same time, properties of metamaterials rely on strong electromagnetic resonances and, consequently, experimental demonstrations of their functionality and their subsequent applications are restricted to narrow spectral intervals determined by the overlap of the desired electric and magnetic response. Active spectral tuning of the metamaterial resonance then appears as a highly desirable property of functional structures.

In a majority of the reported works the tuning or switching of metamaterial properties is generally achieved by a modification of the capacitance of a suitable meta-atom. This can be achieved by a change in the conductivity of the material (semiconductor) which forms the capacitor pads or which fills the space between the capacitor pads [8]. Another possibility is a change of the permittivity of the material forming the capacitor. The external control parameter (electric field, illumination, temperature, or magnetic field) then modifies either the amplitude (strength) of the resonance or its spectral position [31]. In all-dielectric metamaterials the control of the metamaterial response can then be obtained by a tuning of the dielectric permittivity of one (e.g. ferroelectric, high permittivity) component. Recently, a notion of reconfigurable anisotropic metamaterial was introduced where the modulation of the resonance is due to meta-atoms reoriented with respect to the incoming radiation in response to an external control parameter [69].

The first step in the active control of the metamaterial resonant response direction was made by Chen et al. [8] who demonstrated an active planar metamaterial device with a real-time control of a purely electrical resonant response by a low applied volt-

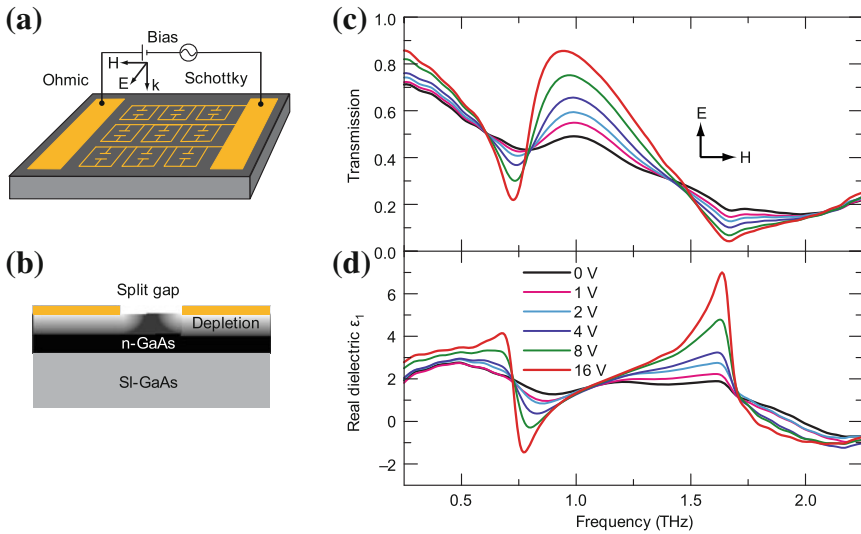
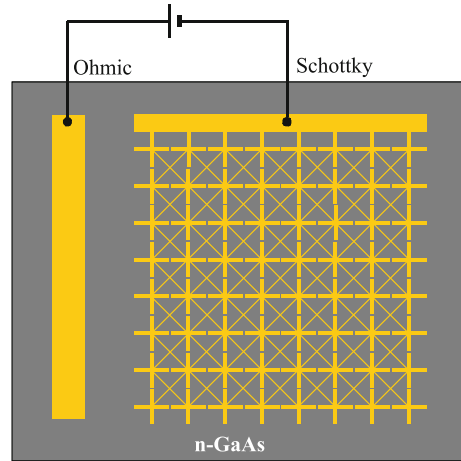


Fig. 22.9 Planar electrically resonant metamaterial for THz light modulation. **a** Scheme of the structure: the metamaterial elements are patterned with a period of $50\ \mu\text{m}$ to form a planar array of $5 \times 5\ \text{mm}^2$. A voltage bias applied between the Schottky and ohmic contacts controls the substrate charge carrier density near the split gaps, tuning the strength of the resonance. **b** Diagram of the substrate and the depletion region near the split gap, where the grayscale indicates the free charge carrier density. **c** Frequency-dependent transmitted intensity of THz radiation and **d** the corresponding permittivity for various reverse gate biases. After [8]

age. The device consisted of an array of gold resonator elements with a symmetry not allowing the magnetic response. The metallic structures were deposited on a $1\ \mu\text{m}$ thick moderately n -doped GaAs layer. The metal and n -GaAs form a Schottky junction and the conductively connected metamaterial resonators serve as a metallic gate (Fig. 22.9). Without an applied voltage the split-gap capacitors are short circuited by the conductive substrate; upon application of a voltage, a resonant behavior appears resulting from a restored capacitance of the split-gap: due to an electrostatic force the carriers in the substrate below and near the metallic pads are displaced and a depleted layer is created, i.e., the conductive connection mediated by the carriers is broken (see Fig. 22.9). The transmission function of such a planar device strongly depends on the presence of the resonance near 1 THz which is controlled by an applied bias 0–16 V and a power modulation of up to 50% has been observed at $\sim\text{kHz}$ modulation frequencies [8]. A multipixel spatial modulator for THz beams was proposed later based on the above described split-ring arrays assembled into a 4×4 pixel matrix where each pixel of $1 \times 1\ \text{mm}^2$ was controlled independently by an external voltage [111].

Electromagnetic properties like resonant surface current density and local electric field distribution of the nonmagnetic split-ring-based planar metamaterials with various symmetries have been studied by the same group in subsequent papers in view

Fig. 22.10 Schematic layout of the cross structure with externally tunable bias supply for modulation of the THz light, after [115]



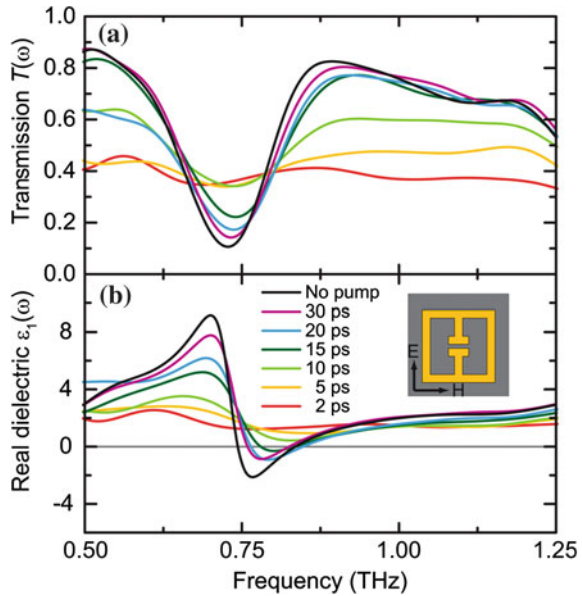
of tailoring their response [65, 112, 113]. The phase modulation of the THz radiation has been recently demonstrated by using similar principle and similar metamaterial structures [114].

A modified design of the metamaterial pattern has been proposed by Paul et al. [115] in order to obtain a polarization-independent response. This device operates on the same principle of Schottky contact and depletion layer as described above. The active layer consists of gold crosses deposited on *n*-doped GaAs layer (see Fig. 22.10). An amplitude modulation of up to 30 % has been achieved by means of control bias voltage with modulation frequencies not exceeding 100 kHz.

The same principle of carrier depletion in a Schottky diode structure was used to achieve an electronic control of extraordinary transmission of THz radiation through subwavelength metal hole arrays [67]. The metal hole arrays were deposited by photolithography on a 2 μm thick moderately *n*-doped GaAs layer. Without external bias the transmission through the holes is significantly decreased (as compared to that of a structure deposited directly on semi-insulating GaAs without the doped layer) due to the conductivity of free carriers in the *n*-doped layer. Upon applying a reverse voltage the transparency of the structure for the THz radiation increases at resonant frequencies; this demonstrates the restoring of extraordinary transmission effect with increasing depletion area in the holes.

Optical switching of a THz metamaterial has been first demonstrated by Padilla et al. [116] and subsequently, on a picosecond timescale, by Chen et al. [117]. Here, a nonmagnetic metallic metamaterial pattern (similar to that shown in Fig. 22.9) is deposited on an undoped semiconductor. Without illumination (in the ground state) the meta-atom shows a resonance in the sub-THz range (0.75 THz in [117]) owing to the capacitance of the split-gap which leads to a low transmittance of the structure close to the resonant frequency. The optically controlled switching has an advantage of a possible ultrafast response of the structure demonstrated in [117]. In order to achieve this, ErAs/GaAs superlattices have been grown by molecular beam

Fig. 22.11 Transmittance and real part of the dielectric function of a metamaterial with a motive shown in the inset deposited on ErAs/GaAs superlattice. Free carriers are injected into the semiconductor by photoexcitation; evolution of the spectra on the picosecond timescale after photoexcitation is shown. After [117]



epitaxy on top of a semi-insulating GaAs substrate below the metamaterial structure. The conductivity of the semiconductor structure is switched on by photoinjection of electrons into the conduction band of GaAs by using a femtosecond optical pulse at 800 nm. A carrier concentration of about $4 \times 10^{16} \text{ cm}^{-3}$ is sufficient to shunt the capacitive regions of the metamaterial pattern destroying the metamaterial resonance; consequently, the THz transmittance of the structure is increased under illumination by about 50% [117]. The free carrier lifetime is ultrashort (in the picosecond and subpicosecond range) and it can be tuned by changing the period of the superlattice [118]; the parameters of the superlattice in Ref. [117] were chosen such that the low THz transmittance of the metamaterial is recovered within 20 ps (see Fig. 22.11). Similar experiments were also made with double-ring resonator structures deposited on a high-resistivity silicon substrate [119] and experiments without the time resolution of the modulation were carried out with classical double SRRs deposited on high-resistivity GaAs [120].

An optically induced tuning of the metamaterial resonant frequency has been demonstrated in [78]. Here, the gold split-rings, with the same geometrical form as those in [8] and [117], were deposited on sapphire. The capacitor plates of the split ring were partly made of a high-resistivity silicon film; this allowed the authors to control their conductivity by optical excitation of charge carriers in silicon. In this manner the split-ring capacitance dependent on the size of conducting capacitor pads could be dynamically controlled by illumination with amplified laser pulses. An optical switching of the metamaterial resonance between 0.85 and 1.05 THz has been observed.

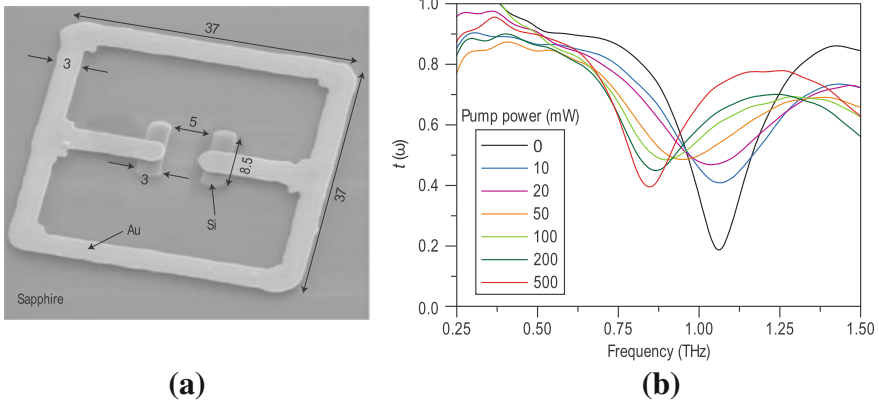


Fig. 22.12 **a** Scanning electron microscopy image of the unit cell of optically frequency-tunable planar metamaterial. Dimensions are in micrometers. **b** Terahertz electric-field transmission amplitude of the metamaterial measured by TDTS. After [78]

A metamaterial electrically resonant (non-magnetic) split-ring structure deposited on a dielectric substrate has been recently proposed consisting of three capacitor gaps, two of them being filled with a suitable semiconductor layer [121]. The calculations were made for silicon. If an optical pulse excites the silicon film the two capacitors are shunted. This significantly changes the effective LC term of the meta-atom and the resonant frequency is displaced from 0.7 to 1 THz in the presented simulations [121]. The idea of dual electrically resonant meta-atoms with two different split-gaps has been experimentally demonstrated in the THz range previously [122].

The capacitance of the SRRs has been also tuned by changing the permittivity in the split-gap of the capacitor: the authors of [123] used drops of silicon nanospheres diluted in ethanol to influence reversibly the resonance frequency of SRR-based metamaterial by up to 10%.

The temperature tuning of metamaterial resonances has been also demonstrated. In a dielectric metamaterial composed of an array of high-permittivity SrTiO_3 rods (see Fig. 22.5a) a tunable negative effective permeability was achieved due to the temperature-dependent permittivity of SrTiO_3 which defines the resonant confinement of the THz radiation inside the rods [31]. The range, where the negative permeability was achieved, was tuned between 0.2 and 0.4 THz. The permittivity of SrTiO_3 is in principle tunable by electric field in the THz spectral range [124, 125]; however, the electric-field tuning of the effective magnetic permeability in this metamaterial structure has not been experimentally demonstrated, yet. A tunable dielectric (or ferroelectric) can be also used as a substrate for metallic metamaterial resonant elements. In this case the tuning of the resonant frequency is achieved through a modification of the dielectric permittivity of the substrate between the capacitor pads of the metamaterial resonator; a thermal tuning of such a planar metamaterial deposited on an SrTiO_3 single crystal substrate has been recently achieved [126]. The dramatic

change of the inductance and resistance of a material close to the superconducting phase transition was used to tune thermally a metamaterial based on niobium nitride (NbN) superconductor [127]. Electric-SRRs were fabricated from a thin NbN layer (deposited on MgO substrate by RF magnetron sputtering) using a photolithography and reactive ion etching. The electric resonances of the planar metamaterial then exhibited an appreciable frequency change and sharpening upon thermal switching between the normal and superconducting state [127].

The thermal tunability of VO₂ cut-wires has been also demonstrated in the THz spectral range [94]. Thermal triggering of the insulator–metal transition (temperature change between 300 and 340 K) leads to an increase in the conductivity of VO₂ wires and, consequently, to a 65 % change of the THz transmittance of the metamaterial layer.

Although a magnetic metamaterial tunability has not been reported in the THz range, a magnetically tunable negative refractive index was observed in the microwave range by He et al. [128] by taking advantage of magnetic properties of a ferrite. Recently, an electrically resonant THz metamaterial controlled by an external magnetic field has been demonstrated [129]. Here, the split-gap capacitor of an electric-SRR similar to that shown in the inset of Fig. 22.11b was replaced by a parallel plate capacitor; one capacitor plate was sustained by a flexible cantilever beam coated with a magnetic thin-film. This allowed the authors to tune the metamaterial resonance by bending the cantilever in an externally applied magnetic field [130].

Finally, reconfigurable anisotropic metamaterials based on SRRs have been proposed and demonstrated recently [69]. Planar arrays of SRRs are fabricated on bimaterial cantilevers designed to bend out-of-plane in response to a thermal stimulus, Fig. 22.7b. The magnetic response of the split-ring is component of the magnetic field vector perpendicular to the split-ring plane. The control of the orientation of the split rings with respect to the magnetic field of the incoming THz radiation then provides a mean for the modulation of the effective magnetic response of the structure.

22.6.3 Other Applications

The interaction of radiation with metamaterials is very strong close to the resonances, therefore it is interesting to study the possibility to conceive metamaterial-based absorbers. This concept is expected to be especially fruitful at THz frequencies where it is difficult to find strong natural absorbing elements. An ideal absorber is obtained if both reflectance and transmittance of a designed absorptive sheet are equal to 0. It follows from Eq. (22.23) that the reflectivity vanishes if $Z = 1$ (no impedance mismatch with the surrounding air). The transmission then exponentially decreases with kd , where k is the effective absorptive index of the sheet and d is the sheet thickness. It means that, in contrast to other targeted applications of metamaterials, for this particular field of research it is desirable to maximize the effective loss k of the metamaterial. This is a direction of the metamaterial research that has received attention only in few works up to now [130–133]. The structure consists in general

of two planes with metallic patterns separated by a thin dielectric sheet. The shape of the patterns then essentially defines the effective dielectric permittivity and the combination of the two patterns results in an effective magnetic response due to circulating currents between the two layers. The magnetic response then can be quasi-independently tuned by the distance between the two layers. Electrically resonant meta-atoms were chosen for the first layer, while cut-wires [130] or a continuous metallic sheet [131] or metallic crosses [132] were selected for the second one. The best performance was achieved in the geometry with the continuous metallic sheet for which an absorptivity exceeding 95% was experimentally obtained at the resonant frequency.

Antireflective coatings were proposed based on fabrication of metamaterial-based slabs with on-demand refractive indices and negligible absorption. These structures were made either by deep reactive plasma etching of silicon [17, 19, 20] or by stacking of metal meshes embedded in dielectric substrate [134].

Metamaterials frequently display a high artificial birefringence which can then be utilized in the manipulation of polarization of the THz radiation. A birefringence of up to 1.25 can be achieved in silicon walls over a thickness of $\sim 80 \mu\text{m}$ obtained by reactive plasma etching [18]. Peralta et al. [135] have designed and experimentally studied electrically resonant elliptical SRRs which show high in-plane anisotropy (frequency shift in the resonance position). Such components can be used in THz polarimetric devices and for example as birefringent wave plates. Quarter-wave plates based on electrically resonant metamaterials were demonstrated in [136] between 0.6 and 0.7 THz. Half- and quarter-wave plates based on negative refractive index were demonstrated by Weis et al. [137]; these devices are based on cut-wire-pair metamaterials and exhibit refractive indices of opposite signs for orthogonal polarizations. In contrast, for many applications, metamaterials are sought with a high-Q resonant behavior which is not affected by the angle of incidence and the polarization of the incoming wave. Such structures for the THz range have been recently proposed with a unit cell consisting of two concentric resonators with interdigitated fingers placed between the rings [138].

Slowing down the light can simplify optical data processing and storage. In conventional approaches, the light is slowed down by means of coherent excitation of electronic states. Such a scheme imposes severe constraints, including narrow bandwidth, limited working wavelengths, and a strong temperature dependence [99, 139]. An alternative approach has been recently proposed and consists in the development of optical meta-structures [140]. The authors theoretically proposed a left-handed heterostructure for the THz range, where a negative-refractive-index core with gradually decreasing thickness is surrounded by positive-refractive-index cladding. The beam in the negative-refractive-index layer propagates in a zigzag fashion and experiences negative Goos-Hänchen lateral displacements on the core-cladding interface [141]. For a suitable core thickness, the beam propagation will be compensated by the Goos-Hänchen shift and the light will finally stop. The critical thickness depends on the frequency of radiation which means that the gradually decreasing thickness of the core permits a broadband operation. An analogous proposition by Gan et al. is based on slowing surface plasmon polaritons in a graded metallic

grating [99]. Their group velocity vanishes at cutoff frequency which is determined by the groove height. The grading then again allows a broadband operation as different frequency components are stopped at different places in the structure. A strong reduction in the group velocity was achieved experimentally in a metamaterial structure made of concentric split- and closed rings [82]. The structure was designed in such a way that both rings exhibit the same resonant frequencies, but with significantly different quality factors. This leads to a narrow window of transparency in a broad absorption band which is associated with a strong reduction in the group velocity.

22.7 Concluding Remarks

The terahertz spectroscopy and the metamaterial science are both very new disciplines; this enabled them to meet each other during the phase of a very fast development before their maturity. On the one hand, the THz domain bridges the microwave and optical spectral regions and the THz spectroscopy provides some interesting experimental possibilities (phase sensitivity, near-field spectroscopy): in this sense it significantly contributes to the boost of the metamaterial research development. On the other hand, metamaterial structures with specific response and behavior are now demanded in order to allow more convenient spatial and temporal control of THz waves with devices aiming at industrial applications. It is hoped that the topics and examples discussed in this chapter do evince an intense interaction between these two fields of research and provide an impression of what can still be discovered.

The length scales are such that the technologies of elaboration of appropriately sized structures become mature. The latest technological trends involve efforts in developing 3D metamaterials and in introducing cheap technologies of metamaterial production. Patterned metals, semiconductors, and high-permittivity dielectrics (ferroelectrics) are currently used for the development of various structures which allow control of the strength of the interaction between the THz light and the metamaterial device. Namely, the optical and electric control of the conduction band carriers in semiconductor micro- and nanostructures and the temperature and electric-field control of the permittivity in ferroelectric inclusions provide the basis for the modulation of the resonant interactions. As it follows from the above text, significant progress has been achieved in understanding these interactions and in designing new operating devices. Nevertheless, the field for the optimization of these structures and for further research still remains vast and especially the transfer of the ideas and technologies from the laboratory to the industry for real-world applications has barely started.

References

1. V.G. Veselago, Electrodynamics of substances with simultaneously negative values of ϵ and μ . *Sov. Phys. Usp.* **10**, 509–514 (1968)
2. J.B. Pendry, A.J. Holden, W.J. Stewart, Extremely low frequency plasmons in metallic mesostructures. *Phys. Rev. Lett.* **76**, 4773–4776 (1996)
3. J.B. Pendry, A.J. Holden, D.J. Robbins, W.J. Stewart, Low frequency plasmons in thin-wire structures. *J. Phys. Condens. Matter* **10**, 4785 (1998)
4. J.B. Pendry, A.J. Holden, D.J. Robins, W.J. Stewart, Magnetism from conductors and enhanced nonlinear phenomena. *IEEE Trans. Microw. Theory Tech.* **47**, 2075–2084 (1999)
5. J.B. Pendry, Negative refraction makes a perfect lens. *Phys. Rev. Lett.* **85**, 3966–3969 (2000)
6. D.R. Smith, W.J. Padilla, D.C. Vier, S.C. Nemat-Nasser, S. Schultz, Composite medium with simultaneously negative permeability and permittivity. *Phys. Rev. Lett.* **84**, 4184 (2000)
7. T.J. Yen, W.J. Padilla, N. Fang, D.C. Vier, D.R. Smith, J.B. Pendry, D.N. Basov, X. Zhang, Terahertz magnetic response from artificial materials. *Science* **303**, 1494 (2004)
8. H.-T. Chen, W.J. Padilla, J.M.O. Zide, A.C. Gossard, A.J. Taylor, R.D. Averitt, Active terahertz metamaterial devices. *Nature* **444**, 597–600 (2006)
9. R. Marqués, F. Martín, M. Sorolla, *Metamaterials with Negative Parameters* (Wiley, New York, 2008)
10. S.A. Ramakrishna, T.M. Grzegorzczuk, *Physics and applications of negative refractive index materials*, (CRC Press, Boca Raton, 2009)
11. W. Cai, V. Shalaev, *Optical metamaterials*, (Springer, New York, 2010)
12. H.-T. Chen, J.F. O’Hara, A.K. Azad, A.J. Taylor, Manipulation of terahertz radiation using metamaterials. *Laser Photonics Rev.* **5**, 513–533 (2011)
13. L.D. Landau, E.M. Lifshitz, L.P. Pitaevskii, *Electrodynamics of Continuous Media*, (Butterworth-Heinemann, Oxford, 1984)
14. J.D. Jackson, *Classical electrodynamics* (Wiley, Hoboken, 1998)
15. J.C. Maxwell Garnett, Colours in metal glasses and in metallic films. *Phil. Trans. R. Soc.* **203**, 385–420 (1904)
16. D.A.G. Bruggeman, Calculation of various physics constants in heterogenous substances. *Annalen Der Physik* **24**, 636–664 (1935)
17. C. Brückner, T. Käsebier, B. Pradarutti, S. Riehemann, G. Notni, E.-B. Kley, A. Tünnermann, Broadband antireflective structures applied to high resistive float zone silicon in the THz spectral range. *Opt. Express* **17**, 3063–3077 (2009)
18. C. Kadlec, F. Kadlec, P. Kuzel, K. Blary, P. Mounaix, Materials with on-demand refractive indices in the terahertz range. *Opt. Lett.* **33**, 2275–2277 (2008)
19. S. Biber, D. Schneiderbanger, L.-P. Schmidt, Design of a controllable attenuator with high dynamic range for THz-frequencies based on optically stimulated free carriers in high-resistivity silicon. *Frequenz* **59**, 141–144 (2005)
20. Y.W. Chen, P.Y. Han, X.-C. Zhang, Three-dimensional inverted photonic grating with engineerable refractive indices for broadband antireflection of terahertz waves. *Opt. Lett.* **35**, 3159–3161 (2010)
21. Y. Zheng, A. Johnson, E. Pyde, K.J. Chau, Particle-size effects on the terahertz transmittance of metallic particle ensembles: comparison with effective medium theory. *Appl. Phys. Lett.* **96**, 211111 (2010)
22. H.-K. Nienhuys, V. Sundström, Influence of plasmons on terahertz conductivity measurements. *Appl. Phys. Lett.* **87**, 012101 (2005)
23. H. Nemeč, P. Kuzel, V. Sundström, Charge transport in nanostructured materials for solar energy conversion studied by time-resolved terahertz spectroscopy. *J. Photochem. Photobiol. A* **215**, 123–139 (2010)
24. E. Hendry, M. Koeberg, B. O’Regan, M. Bonn, Local field effects on electron transport in nanostructures TiO₂ revealed by terahertz spectroscopy. *Nano Lett.* **6**, 755–759 (2006)
25. K.J. Button, *Infrared and Millimeter Waves, Millimeter components and techniques*, Chap. 6, vol. 13 (Academic, New York, 1985), pp. 175–185

26. Y. Zheng, A. Johnson, E. Pyde, K.J. Chau, Particle-size effects on the terahertz transmittance of metallic particle ensembles: Comparison with effective medium theory. *Appl. Phys. Lett.* **96**, 211111 (2010)
27. M. Walther, D.G. Cooke, C. Sherstan, M. Hajar, M.R. Freeman, F.A. Hegmann, Terahertz conductivity of thin gold films at the metal-insulator percolation transition. *Phys. Rev. B* **76**, 125408 (2007)
28. G. Mie, Beiträge zur Optik trüber Medien, speziell kolloidaler Metallösungen. *Ann. Phys.* **25**, 376–445 (1908)
29. S. O'Brien, J.B. Pendry, Photonic band-gap effects and magnetic activity in dielectric composites. *J. Phys. Condens. Matter* **14**, 4035–4044 (2002)
30. V. Yannopapas, A. Moroz, Negative refractive index metamaterials from inherently non-magnetic materials for deep infrared to terahertz frequency ranges. *J. Phys. Condens. Matter* **17**, 3717–3734 (2005)
31. H. Nemeč, P. Kuzel, F. Kadlec, C. Kadlec, R. Yahiaoui, and P. Mounaix, Tunable terahertz metamaterials with negative permeability. *Phys. Rev. B* **79**, 241108(R) (2009)
32. Q. Zhao, L. Kang, B. Du, H. Zhao, Q. Xie, X. Huang, B. Li, J. Zhou, L. Li, Experimental demonstration of isotropic negative permeability in a three-dimensional dielectric composite. *Phys. Rev. Lett.* **101**, 027402 (2008)
33. K. Vynck, D. Felbacq, E. Centeno, A.I. Cabuz, D. Cassagne, B. Guizal, All-dielectric rod-type metamaterials at optical frequencies. *Phys. Rev. Lett.* **102**, 133901 (2009)
34. A. Bitzer, J. Wallauer, H. Helm, H. Merbold, T. Feurer, M. Walther, Lattice modes mediate radiative coupling in metamaterial arrays. *Opt. Express* **17**, 22108–22113 (2009)
35. R. Singh, C. Rockstuhl, F. Lederer, W. Zhang, The impact of nearest neighbor interaction on the resonances in terahertz metamaterials. *Appl. Phys. Lett.* **94**, 021116 (2009)
36. D.R. Chowdhury, R. Singh, M. Reiten, J. Zhou, A.J. Taylor, J.F. O'Hara, Tailored resonator coupling for modifying the terahertz metamaterial response. *Opt. Express* **19**, 10679–10685 (2011)
37. M.N.O. Sadiku, *Numerical Techniques in Electromagnetics*, 2nd ed. (CRC Press LLC, Boca Raton, 2001)
38. <http://www.ansoft.com/>
39. <http://www.cst.com/>
40. J.B. Pendry, A. MacKinnon, Calculation of photon dispersion relations. *Phys. Rev. Lett.* **69**, 2772–2775 (1992)
41. J.B. Pendry, Photonic band structures. *J. Mod. Opt.* **41**, 209–229 (1994)
42. P. Markoš, C.M. Soukoulis, Numerical studies of left-handed materials and arrays of split ring resonators. *Phys. Rev. E* **65**, 036622 (2002)
43. D.R. Smith, S. Schultz, P. Markoš, C.M. Soukoulis, Determination of effective permittivity and permeability of metamaterials from reflection and transmission coefficients. *Phys. Rev. B* **65**, 195104 (2002)
44. S. Zhang, W. Fan, K.J. Malloy, S.R. Brueck, N.C. Panoiu, R.M. Osgood, Near-infrared double negative metamaterials. *Opt. Express* **13**, 4922–4930 (2005)
45. M.G. Maharam, T.K. Gaylord, Rigorous coupled-wave analysis of planar-grating diffraction. *J. Opt. Soc. Am.* **71**, 811–818 (1981)
46. T.F. Gundogdu, N. Katsarakis, M. Kafesaki, R.S. Penciu, G. Konstantinidis, A. Kostopoulos, E.N. Economou, C.M. Soukoulis, Negative index short-slab pair and continuous wires metamaterials in the far infrared regime. *Opt. Express* **16**, 9173–9180 (2008)
47. N. Katsarakis, G. Konstantinidis, A. Kostopoulos, R.S. Penciu, T.F. Gundogdu, M. Kafesaki, E.N. Economou, Th Koschny, C.M. Soukoulis, Magnetic response of split-ring resonators in the far-infrared frequency regime. *Opt. Lett.* **30**, 1348–1350 (2005)
48. W.J. Padilla, D.R. Smith, D.N. Basov, Spectroscopy of metamaterials from infrared to optical frequencies. *J. Opt. Soc. Am. B* **23**, 404–414 (2006)
49. T.F. Gundogdu, I. Tsiapa, A. Kostopoulos, G. Konstantinidis, N. Katsarakis, R.S. Penciu, M. Kafesaki, E.N. Economou, Th Koschny, C.M. Soukoulis, Experimental demonstration of negative magnetic permeability in the far-infrared frequency regime. *Appl. Phys. Lett.* **89**, 084103 (2006)

50. T. Driscoll, G.O. Andreev, D.N. Basov, S. Palit, T. Ren, J. Mock, S.-Y. Cho, N.M. Jokerst, D.R. Smith, Quantitative investigation of a terahertz artificial magnetic resonance using oblique angle spectroscopy. *Appl. Phys. Lett.* **90**, 092508 (2007)
51. Y. Minowa, T. Fujii, M. Nagai, T. Ochiai, K. Sakoda, K. Hirao, K. Tanaka, Evaluation of effective electric permittivity and magnetic permeability in metamaterial slabs by terahertz time-domain spectroscopy. *Opt. Express* **16**, 4785–4796 (2008)
52. M. Awad, M. Nagel, H. Kurz, Negative-index metamaterial with polymer-embedded wire-pair structures at terahertz frequencies. *Opt. Lett.* **33**, 2683–2685 (2008)
53. A. Bitzer, H. Merbold, A. Thoman, T. Feurer, H. Helm, M. Walther, Terahertz near-field imaging of electric and magnetic resonances of a planar metamaterial. *Opt. Express* **17**, 3826–3834 (2009)
54. Ch. Menzel, C. Rockstuhl, F. Lederer, Advanced Jones calculus for the classification of periodic metamaterials. *Phys. Rev. A* **82**, 053811 (2010)
55. R. Singh, E. Plum, C. Menzel, C. Rockstuhl, A.K. Azad, R.A. Cheville, F. Lederer, W. Zhang, N.I. Zheludev, Terahertz metamaterial with asymmetric transmission. *Phys. Rev. B* **80**, 153104 (2009)
56. D.R. Smith, D.C. Vier, Th Koschny, C.M. Soukoulis, Electromagnetic parameter retrieval from inhomogeneous metamaterials. *Phys. Rev. E* **71**, 036617 (2005)
57. T. Driscoll, D.N. Basov, W.J. Padilla, J.J. Mock, D.R. Smith, Electromagnetic characterization of planar metamaterials by oblique spectroscopic measurements. *Phys. Rev. B* **75**, 115114 (2007)
58. A. Pashkin, M. Kempa, H. Nemeč, F. Kadlec, P. Kužel, Phase-sensitive time-domain terahertz reflection spectroscopy. *Rev. Sci. Instrum.* **74**, 4711–4717 (2003)
59. L. Duvillaret, F. Garet, J.-L. Coutaz, A Reliable Method for Extraction of Material Parameters in Terahertz Time-Domain Spectroscopy. *IEEE J. Sel. Top. Quantum Electron.* **2**, 739–746 (1996)
60. H. Nemeč, F. Kadlec, P. Kužel, L. Duvillaret, J.-L. Coutaz, Independent determination of the complex refractive index and wave impedance by time-domain terahertz spectroscopy. *Opt. Commun.* **260**, 175–183 (2006)
61. P. Uhd Jepsen, D.G. Cooke, M. Koch, Terahertz spectroscopy and imaging - Modern techniques and applications. *Laser Photon. Rev.* **5**, 124–166 (2011)
62. W.J. Padilla, M.T. Aronsson, C. Highstrete, M. Lee, A.J. Taylor, R.D. Averitt, Electrically resonant terahertz metamaterials: Theoretical and experimental investigations. *Phys. Rev. B* **75**, 041102 (2007)
63. M.A. Seo, A.J.L. Adam, J.H. Kang, J.W. Lee, S.C. Jeoung, Q.H. Park, P.C.M. Planken, D.S. Kim, Fourier-transform terahertz near-field imaging of one-dimensional slit arrays: mapping of electric-field-, magnetic-field-, and Poynting vectors. *Opt. Express* **15**, 11781–11789 (2007)
64. A.K. Azad, J. Dai, W. Zhang, Transmission properties of terahertz pulses through subwavelength double split-ring resonators. *Opt. Lett.* **31**, 634–636 (2006)
65. W.J. Padilla, M.T. Aronsson, C. Highstrete, M. Lee, A.J. Taylor, R.D. Averitt, Electrically resonant terahertz metamaterials: theoretical and experimental investigations. *Phys. Rev. B* **75**, 041102(R) (2007)
66. H.-T. Chen, S. Palit, T. Tyler, C.M. Bingham, J.M.O. Zide, J.F. O'Hara, D.R. Smith, A.C. Gossard, R.D. Averitt, W.J. Padilla, N.M. Jokerst, A.J. Taylor, Hybrid metamaterials enable fast electrical modulation of freely propagating terahertz waves. *Appl. Phys. Lett.* **93**, 091117 (2008)
67. H.-T. Chen, H. Lu, A.K. Azad, R.D. Averitt, A.C. Gossard, S.A. Trugman, J. F. O'Hara, and A. J. Taylor, Electronic control of extraordinary terahertz transmission through subwavelength metal hole arrays. *Opt. Express* **16**, 7641–7648 (2008)
68. D. Wu, N. Fang, C. Sun, X. Zhang, Terahertz plasmonic high pass filter. *Appl. Phys. Lett.* **83**, 201–203 (2003)
69. H. Tao, A.C. Strikwerda, K. Fan, W.J. Padilla, X. Zhang, R.D. Averitt, Reconfigurable terahertz metamaterials. *Phys. Rev. Lett.* **103**, 147401 (2009)

70. M. Aznabet, M. Navarro-Cía, S.A. Kuznetsov, A.V. Gelfand, N.I. Fedorinina, YuG Goncharov, M. Beruete, O. El Mrabet, M. Sorolla, Polypropylene-substrate-based SRR- and CSRR- meta-surfaces for submillimeter waves. *Opt. Express* **16**, 18312–18319 (2008)
71. H. Tao, A.C. Strikwerda, K. Fan, C.M. Bingham, W.J. Padilla, X. Zhang, R.D. Averitt, Terahertz metamaterials on free-standing highly-flexible polyimide substrates. *J. Phys. D: Appl. Phys.* **41**, 232004 (2008)
72. X. Liu, S. MacNaughton, D.B. Shrekenhamer, H. Tao, S. Selvarasah, A. Totachawattana, R.D. Averitt, M.R. Dokmeci, S. Sonkusale, W.J. Padilla, Metamaterials on parylene thin film substrates: Design, fabrication, and characterization at terahertz frequency. *Appl. Phys. Lett.* **96**, 011906 (2010)
73. H. Tao, J.J. Amsden, A.C. Strikwerda, K. Fan, D.L. Kaplan, X. Zhang, R.D. Averitt, F.G. Omenetto, Metamaterial silk composites at terahertz frequencies. *Adv. Mater.* **22**, 3527–3531 (2010)
74. N.R. Han, Z.C. Chen, C.S. Lim, B. Ng, M.H. Hong, Broadband multi-layer terahertz metamaterials fabrication and characterization on flexible substrates. *Opt. Express* **19**, 6990–6998 (2011)
75. H.O. Moser, J.A. Kong, L.K. Jian, H.S. Chen, G. Liu, M. Bahou, S.M.P. Kalaiselvi, S.M. Maniam, X.X. Cheng, B.I. Wu, P.D. Gu, A. Chen, S.P. Heussler, S. bin Mahnood, and L. Wen, Free-standing THz electromagnetic metamaterials. *Opt. Express* **16**, 13773–13780 (2008)
76. B.D.F. Casse, H.O. Moser, J.W. Lee, M. Bahou, S. Inglis, L.K. Jian, Towards three-dimensional and multilayer rod-split-ring metamaterial structures by means of deep x-ray lithography. *Appl. Phys. Lett.* **90**, 254106 (2007)
77. S. Linden, C. Enkrich, M. Wegener, J. Zhou, T. Koschny, C.M. Soukoulis, Magnetic response of metamaterials at 100 terahertz. *Science* **306**, 1351–1353 (2004)
78. H.-T. Chen, J.F. O'Hara, A.K. Azad, A.J. Taylor, R.D. Averitt, D.B. Shrekenhamer, W.J. Padilla, Experimental demonstration of frequency-agile terahertz metamaterials. *Nature Photon.* **2**, 295–298 (2008)
79. S.C. Saha, Y. Ma, J.P. Grant, A. Khalid, D.R.S. Cumming, Imprinted terahertz artificial dielectric quarter wave plates. *Opt. Express* **18**, 12168–12175 (2010)
80. H.O. Moser, B.D.F. Casse, O. Wilhelmi, B.T. Saw, Terahertz response of a microfabricated rod-split-ring-resonator electromagnetic metamaterial. *Phys. Rev. Lett.* **94**, 063901 (2005)
81. M.S. Rill, C. Plet, M. Thiel, I. Staude, G. von Freymann, S. Linden, M. Wegener, Photonic metamaterials by direct laser writing and silver chemical vapour deposition. *Nature Mat.* **7**, 543–546 (2008)
82. S.Y. Chiam, R. Singh, C. Rockstuhl, F. Lederer, W. Zhang, A.A. Bettiol, Analogue of electromagnetically induced transparency in a terahertz metamaterial. *Phys. Rev. B* **80**, 153103 (2009)
83. R. Yahiaoui, H. Nemeč, P. Kuzel, F. Kadlec, C. Kadlec, P. Mounaix, Broadband dielectric terahertz metamaterials with negative permeability. *Opt. Lett.* **34**, 3541 (2009)
84. C. Kang, C.-S. Kee, I.-B. Sohn, J. Lee, Characterization of terahertz wave transmission through complementary metamaterials with split ring resonator arrays, in *Abstracts from 34th International conference on Infrared, Millimeter, and Terahertz Waves* (Busan, South Korea, 2009), pp. 767–768
85. T. Kondo, T. Nagashima, M. Hangyo, Fabrication of wire-grid-type polarizers for THz region using a general-purpose color printer. *Jpn. J. Appl. Phys. Part 2* (42), L373–L375 (2003)
86. K. Takano, T. Kawabata, C.-F. Hsieh, K. Akiyama, F. Miyamaru, Y. Abe, Y. Tokuda, R.-P. Pan, C.-L. Pan, M. Hangyo, Fabrication of terahertz planar metamaterials using a super-fine ink-jet printer. *Appl. Phys. Express* **3**, 016701 (2010)
87. M. Wälther, A. Ortner, H. Meier, U. Löffelmann, P.J. Smith, J.G. Korvink, Terahertz metamaterials fabricated by inkjet printing. *Appl. Phys. Lett.* **95**, 251107 (2009)
88. K. Takano, K. Shibuya, K. Akiyama, T. Nagashima, F. Miyamaru, M. Hangyo, A metal-to-insulator transition in cut-wire-grid metamaterials in the terahertz region. *J. Appl. Phys.* **107**, 024907 (2010)

89. D.A. Pawlak, S. Turczynski, M. Gajc, K. Kolodziejak, R. Diduszko, K. Rozniatowski, J. Smalc, I. Vendik, How far are we from making metamaterials by self-organization? The microstructure of highly anisotropic particles with an SRR-like geometry. *Adv. Funct. Mater.* **20**, 1116–1124 (2010)
90. S. Zhang, W. Fan, B.K. Minhas, A. Frauenglass, K.J. Malloy, S.R.J. Brueck, Fabrication of 1D and 2D vertical nanomagnetic resonators. *J. Vac. Sci. Tech. B* **22**, 3327–3330 (2004)
91. A. Tuniz, B.T. Kuhlmeier, R. Lwin, A. Wang, J. Anthony, R. Leonhardt, S.C. Fleming, Drawn metamaterials with plasmonic response at terahertz frequencies. *Appl. Phys. Lett.* **96**, 191101 (2010)
92. F. Miyamaru, M. Wada Takeda, K. Taima, Characterization of terahertz metamaterials fabricated on flexible plastic films: toward fabrication of bulk metamaterials in terahertz region. *Appl. Phys. Express* **2**, 042001 (2009)
93. F. Miyamaru, S. Kuboda, K. Taima, K. Takano, M. Hangyo, M. Wada Takeda, Three-dimensional bulk metamaterials operating in the terahertz range. *Appl. Phys. Lett.* **93**, 081105 (2010)
94. Q.-Y. Wen, H.-W. Zhang, Q.-H. Yang, Y.-S. Xie, K. Chen, Y.-L. Liu, Terahertz metamaterials with VO₂ cut-wires for thermal tunability. *Appl. Phys. Lett.* **97**, 021111 (2010)
95. Y.W. Chen, P.Y. Han, X.-C. Zhang, Tunable broadband antireflection structures for silicon at terahertz frequency. *Appl. Phys. Lett.* **94**, 041106 (2009)
96. S. Zhang, Y.-S. Park, J. Li, X. Lu, W. Zhang, X. Zhang, Negative refractive index in chiral metamaterials. *Phys. Rev. Lett.* **102**, 023901 (2009)
97. A. Pimenov, A. Loidl, Experimental demonstration of artificial dielectrics with a high index of refraction. *Phys. Rev. B* **74**, 193102 (2006)
98. C.R. Williams, S.R. Andrews, S.A. Maier, A.I. Fernández-Domínguez, L. Martín-Moreno, F.J. García-Vidal, Highly confined guiding of terahertz surface plasmon polaritons on structured metal surfaces. *Nature Photon.* **2**, 175–179 (2008)
99. Q. Gan, Z. Fu, Y.J. Ding, F.J. Bartoli, Ultrawide-bandwidth slow-light system based on THz plasmonic graded metallic grating structures. *Phys. Rev. Lett.* **100**, 256803 (2008)
100. A. Ishikawa, S. Zhang, D.A. Genov, G. Bartal, X. Zhang, Deep subwavelength terahertz waveguides using gap magnetic plasmon. *Phys. Rev. Lett.* **102**, 043904 (2009)
101. J. Lee, K. Lee, H. Park, G. Kang, D.-H. Yu, K. Kim, Tunable subwavelength focusing with dispersion-engineered metamaterials in the terahertz regime. *Opt. Lett.* **35**, 2254–2256 (2010)
102. F. Miyamaru, S. Kuboda, K. Taima, K. Takano, M. Hangyo, M.W. Takeda, Three-dimensional bulk metamaterials operating in the terahertz range. *Appl. Phys. Lett.* **96**, 081105 (2010)
103. K. Fan, A.C. Strikwerda, H. Tao, X. Zhang, R.D. Averitt, 3D Stand-up Metamaterials with a Purely Magnetic Resonance at Terahertz Frequencies, in *Proceeding of the 30th Conference on Lasers and Electro-Optics/International Quantum Electronics and Laser Science Conference (CLEO/QELS '10)*, San Jose, CA, USA, CTuF1, 18–20 May 2010
104. K. Fan, A.C. Strikwerda, H. Tao, X. Zhang, R.D. Averitt, Stand-up magnetic metamaterials at terahertz frequencies. *Opt. Express* **19**, 12619–12627 (2011)
105. C.M. Soukoulis, J. Zhou, T. Koschny, M. Kafesaki, E.N. Economou, The science of negative index materials. *J. Phys. Condens. Matter* **20**, 304217 (2008)
106. J. Carbonell, C. Croënne, F. Garet, E. Lheurette, J.L. Coutaz, D. Lippens, Lumped elements circuit of terahertz fishnet-like arrays with composite dispersion. *J. Appl. Phys.* **108**, 014907 (2010)
107. Q. Zhao, J. Zhou, F. Zhang, D. Lippens, Mie resonance-based dielectric metamaterials. *Mat. Today* **12**, 60–69 (2009)
108. P. Kuzel, H. Nemeč, F. Kadlec, Highly tunable structures for the THz range based on strontium titanate heterostructures and metamaterials, in *Proceedings of 2nd International Congress on Advanced Electromagnetic Materials in Microwaves and Optics* (Pamplona, Spain, September, 2008), pp. 21–26
109. K. Shibuya, K. Takano, N. Matsumoto, K. Izumi, H. Miyazaki, Y. Jimba, M. Hangyo, Terahertz metamaterials composed of TiO₂ cube arrays, in *Proceedings of 2nd International Congress on Advanced Electromagnetic Materials in Microwaves and Optics* (Pamplona, Spain, September, 2008), pp. 21–26

110. P. Kuzel, F. Kadlec, Tunable structures and modulators for THz light. *Comptes Rendus Physique* **9**, 197–214 (2008)
111. W.L. Chan, H.-T. Chen, A.J. Taylor, I. Brener, M.J. Cich, A spatial light modulator for terahertz beams. *Appl. Phys. Lett.* **94**, 213511 (2009)
112. H.-T. Chen, J.F. O'Hara, A.J. Taylor, R.D. Averitt, C. Highstrete, M. Lee, W.J. Padilla, Complementary planar terahertz metamaterials. *Opt. Express* **15**, 1084–1095 (2007)
113. A.K. Azad, A.J. Taylor, E. Smirnova, J.F. O'Hara, Characterization and analysis of terahertz metamaterials based on rectangular split-ring resonators. *Appl. Phys. Lett.* **92**, 011119 (2008)
114. H.-T. Chen, W.J. Padilla, M.J. Cich, A.K. Azad, R.D. Averitt, A.J. Taylor, A metamaterial solid-state terahertz phase modulator. *Nature Photon.* **3**, 148–151 (2009)
115. O. Paul, C. Imhof, B. Lagel, S. Wolff, J. Heinrich, S. Hofling, A. Forchel, R. Zengerle, R. Beigang, M. Rahm, Polarization-independent active metamaterial for high-frequency terahertz modulation. *Opt. Express* **17**, 819–827 (2009)
116. W.J. Padilla, A.J. Taylor, C. Highstrete, M. Lee, R.D. Averitt, Dynamical electric and magnetic metamaterial response at terahertz frequencies. *Phys. Rev. Lett.* **96**, 107401 (2006)
117. H.-T. Chen, W.J. Padilla, J.M.O. Zide, S.R. Bank, A.C. Gossard, A.J. Taylor, R.D. Averitt, Ultrafast optical switching of terahertz metamaterials fabricated on ErAs/GaAs nanoislands superlattices. *Opt. Lett.* **32**, 1620–1622 (2007)
118. C. Kadow, S.B. Fleischer, J.P. Ibbetson, J.E. Bowers, A.C. Gossard, J.W. Dong, C.J. Palmstrom, Self-assembled ErAs islands in GaAs: Growth and subpicosecond carrier dynamics. *Appl. Phys. Lett.* **75**, 3548 (1999)
119. Y. Shi, Q. Zhou, W. Liu, J. Liu, C. Zhang, Anomalous transmission of terahertz waves in arrays of double-ring resonators induced by a 400 nm pump pulse. *Appl. Phys. Lett.* **98**, 191112 (2011)
120. J.-M. Manceau, N.-H. Shen, M. Kafesaki, C.M. Soukoulis, S. Tzortzakis, Dynamics response of metamaterials in the terahertz regime: blueshift tunability and broadband phase modulation. *Appl. Phys. Lett.* **96**, 021111 (2010)
121. N.-H. Shen, M. Kafesaki, T. Koschny, L. Zhang, E.N. Economou, C.M. Soukoulis, Broadband blueshift tunable metamaterials and dual-band switches. *Phys. Rev. B* **79**, 161102(R) (2009)
122. Y. Yuan, C. Bingham, T. Tyler, S. Palit, T.H. Hand, W.J. Padilla, N.M. Jokerst, S.A. Cummer, A dual-resonant terahertz metamaterial based on single-particle electric-field-coupled resonators. *Appl. Phys. Lett.* **93**, 191110 (2008)
123. T. Driscoll, G.O. Andreev, D.N. Basov, S. Palit, S.Y. Cho, N.M. Jokerst, D.R. Smith, Tuned permeability in terahertz split-ring resonators for devices and sensors. *Appl. Phys. Lett.* **91**, 062511 (2007)
124. P. Kuzel, F. Kadlec, H. Nemeck, R. Ott, E. Hollmann, N. Klein, Dielectric tunability of SrTiO₃ thin films in the terahertz range. *Appl. Phys. Lett.* **88**, 102901 (2006)
125. C. Kadlec, V. Skorometz, F. Kadlec, H. Nemeck, J. Hlinka, J. Schubert, G. Panaitov, P. Kuzel, Temperature and electric field tuning of the ferroelectric soft mode in a strained SrTiO₃/DyScO₃ heterostructure. *Phys. Rev. B* **80**, 174116 (2009)
126. R. Singh, A.K. Azad, Q.X. Jia, A.J. Taylor, H.-T. Chen, Thermal tunability in terahertz metamaterials fabricated on strontium titanate single-crystal substrates. *Opt. Lett.* **36**, 1230–1232 (2011)
127. J. Wu, B. Jin, Y. Xue, C. Zhang, H. Dai, L. Zhang, C. Cao, L. Kang, W. Xu, J. Chen, P. Wu, Tuning of superconducting niobium nitride terahertz metamaterials. *Opt. Express* **19**, 12021–12026 (2011)
128. G. He, R.-X. Wu, Y. Poo, P. Chen, Magnetically tunable double-negative material composed of ferrite-dielectric and metallic mesh. *J. Appl. Phys.* **107**, 093522 (2010)
129. B. Ozbey, O. Aktas, Continuously tunable terahertz metamaterial employing magnetically actuated cantilevers. *Opt. Express* **19**, 5741–5752 (2011)
130. H. Tao, N.I. Landy, C.M. Bingham, X. Zhang, R.D. Averitt, W.J. Padilla, A metamaterial absorber for the terahertz regime: design, fabrication and characterization. *Opt. Express* **16**, 7181–7188 (2008)

131. H. Tao, C.M. Bingham, A. C. Strikwerda, D. Pilon, D. Shrekenhamer, N.I. Landy, K. Fan, X. Zhang, W. J. Padilla, R. D. Averitt, Highly flexible wide angle of incidence terahertz metamaterial absorber: design, fabrication and characterization. *Phys. Rev. B* **78**, 541103(R) (2008)
132. N.I. Landy, C.M. Bingham, T. Tyler, N. Jokerts, D.R. Smith, W.J. Padilla, Design, theory, and measurement of a polarization-insensitive absorber for terahertz imaging. *Phys. Rev. B* **79**, 125104 (2009)
133. J. Grant, Y. Ma, S. Saha, L.B. Lok, A. Khalid, D.R.S. Cumming, Polarization insensitive terahertz metamaterial absorber. *Opt. Lett.* **36**, 1524–1526 (2011)
134. J. Zhang, P.A.R. Ade, P. Mauskopf, L. Moncelsi, G. Savini, N. Whitehouse, New artificial dielectric metamaterial and its application as a terahertz antireflection coating. *Appl. Opt.* **48**, 6635–6642 (2009)
135. X.G. Peralta, E.I. Smirnova, A.K. Azad, H.-T. Chen, A.J. Taylor, I. Brener, J.F. O’Hara, Metamaterials for THz polarimetric devices. *Opt. Express* **17**, 774–783 (2009)
136. A.C. Strikwerda, K. Fan, H. Tao, D.V. Pilon, X. Zhang, R.D. Averitt, Comparison of birefringent electric split-ring resonator and meanderline structures as quarter-wave plates at terahertz frequencies. *Opt. Express* **17**, 136–149 (2009)
137. P. Weis, O. Paul, C. Imhof, R. Beigang, M. Rahm, Strongly birefringent metamaterials as negative index terahertz wave plates. *Appl. Phys. Lett.* **95**, 171104 (2009)
138. I.A.I. Al-Naib, C. Jansen, N. Born, M. Koch, Polarization and angle independent terahertz metamaterials with high Q-factors. *Appl. Phys. Lett.* **98**, 091107 (2011)
139. L.V. Hau, S.E. Harris, Z. Dutton, C.H. Behroozi, Light speed reduction to 17 metres per second in an ultracold atomic gas. *Nature* **397**, 594 (1999)
140. K.L. Tsakmakidis, A.D. Boardman, O. Hess, Trapped rainbow storage of light in metamaterials. *Nature* **450**, 397–401 (2007)
141. P.R. Berman, Goos-Hänchen shift in negatively refractive media. *Phys. Rev. E* **66**, 067603 (2002)